A comparative study on seismic response of two unstable rock slopes within same tectonic setting but different activity level

Geophysical Journal International

Geophys. J. Int. (2017) **211,** 1428–1448
Advance Access publication 2017 September 11
GJI Seismology

doi: 10.1093/gji/ggx376

A comparative study on seismic response of two unstable rock slopes within same tectonic setting but different activity level

Ulrike Kleinbrod,[1] Jan Burjánek,[1,2] Marc Hugentobler,[1,3] Florian Amann[4] and Donat Fäh[1]

[1]*Swiss Seismological Service, Sonneggstrasse 5, ETH Zürich, CH-8092 Zürich, Switzerland. E-mail: ulrike.kleinbrod@sed.ethz.ch*
[2]*Institute of Geophysics of the CAS, v.v.i., Bocni II/1401, 141 31 Praha 4, Czech Republic*
[3]*Marti Tunnelbau AG, Seedorffeldstrasse 21, CH-3302 Moosseedorf, Switzerland*
[4]*Swiss Competence Center for Energy Research, Sonneggstrasse 5, ETH Zürich, CH-8092 Zürich, Switzerland*

Accepted 2017 September 7. Received 2017 September 6; in original form 2016 December 20

SUMMARY

In this study, the seismic response of two slope instabilities is investigated with seismic ambient vibration analysis. Two similar sites have been chosen: an active deep-seated slope instability at Cuolm da Vi and the geologically, structurally and morphologically similar, but presently not moving Alp Caschlè slope. Both slopes are located at the upper Vorderrheintal (Canton Graubünden, Switzerland). Ambient vibrations were recorded on both slopes and processed by time–frequency polarization and site-to-reference spectral ratio analysis. The data interpretation shows correlations between degree of disintegration of the rock mass and amplification. However, the ambient vibration analysis conducted, does not allow retrieving a resonance frequency that can be related to the total depth of the instability of Cuolm da Vi. Even though seismic waves can be hardly traced in rock instabilities containing open fractures, it was possible to retrieve a dispersion curve and a velocity profile from the array measurement at Cuolm da Vi due to the high level of disintegration of the rock material down to a depth of about 100 m. From the similar amplification pattern at the two sites, we expect a similar structure, indicating that also the slope at Alp Caschlè was active in the past in a similar manner as Cuolm da Vi. However, a smoother increase of amplification with frequency is observed at Alp Caschlè, which might indicate less disintegration of the rock mass in a particular depth range at this site, when comparing to Cuolm da Vi where a high level of disintegration is observed, resulting from the high activity at the slope.

From the frequency-dependent amplification, we can distinguish between two parts within both instabilities, one part showing decreasing disintegration of the rock mass with increasing depth, for the other parts less-fractured blocks are observed. Since the block structures are found in the lower part of the instabilities, they might contribute to the stability of the slopes. Using the velocity profiles, it was possible to estimate the depth of the two largest open fractures (i.e. tension cracks) at Cuolm da Vi.

Key words: Seismic noise; Site effects; Wave propagation.

1 INTRODUCTION

Detecting and characterizing unstable rock slopes based on seismic ambient vibrations is a new technique providing information about the internal structure of the rock mass. Several recent studies revealed distinct seismic response characteristics of unstable slopes such as noise polarization and amplification, both azimuthally and frequency dependent (see Del Gaudio & Wasowski 2010; Burjánek *et al.* 2010a, 2012; Del Gaudio *et al.* 2014). The seismic response of unstable rock slopes is very sensitive to basic geological characteristics such as the type of failure mechanism and kinematic freedom, degree of fracturing, orientation of failure planes and discontinuities, stiffness of the rock mass, etc. Previous measurements at around 25 different sites (see Fig. 1) suggest that based on the seismic response alone, it is not straightforward to compare geologically and morphologically different sites with each other (Kleinbrod *et al.* 2017). Each unstable rock slope has its own specific and very complex seismic response. As a first step, similar geological and morphological features need to be identified to find common patterns at different sites that allow a comparison of the seismic response. Therefore, in this paper, we compare two sites with similar geological and tectonic properties that mainly differ

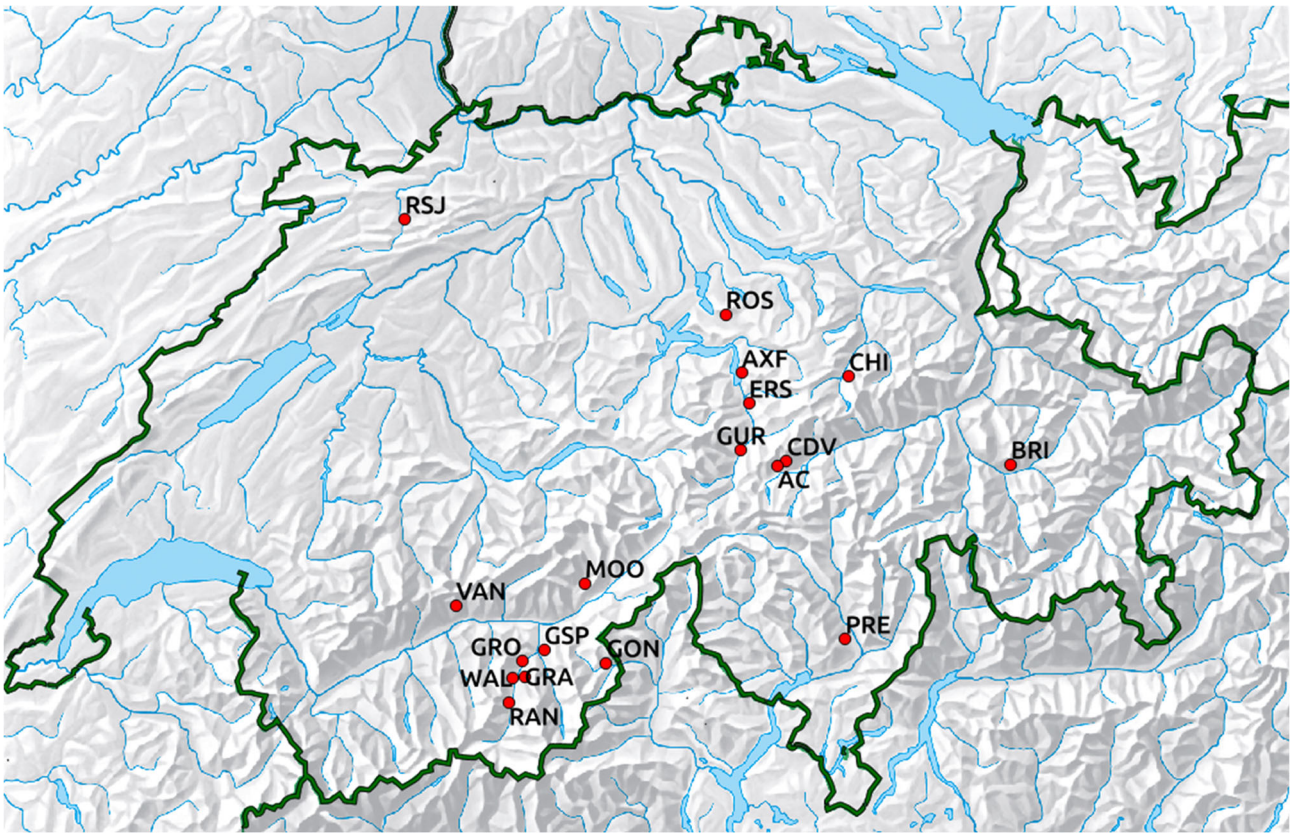

Figure 1. Overview of the measured sites in Switzerland. Around 25 instabilities have been analysed at the indicated locations. Some sites as Axenflue (AXF), Gurtnellen (GUR), Varneralp (VAN), Choindez (RSJ) and Gspon (GSP) comprise measurements at independent subsites.

in their activity level (i.e. rate of displacement). Alp Caschlè is a rock slope that shows evidence for past landslide activities and is currently stable, while Cuolm da Vi is a deep-seated landslide that includes parts that show maximum displacements of up to 90 cm yr^{-1} (Amann 2005; Amann *et al.* 2006).

We study the seismic response of the slopes using ambient vibrations. Methods used for analysing the ambient vibration recordings are polarization analysis (Burjánek *et al.* 2012), site-to-reference spectral ratios (SRSRs), surface wave analysis with array methods including the high-resolution frequency–wavenumber (HRFK) method (Wathelet *et al.* 2008) and subsequent dispersion curve inversion for the *Vs*-velocity profile using the neighbourhood algorithm (Wathelet 2008). One of the key questions is whether fast moving rock slopes show a different seismic response compared to rock slopes without recent displacements. We investigate in which frequency band it is possible to retrieve a dispersion curve on heavily fractured rock slopes. Furthermore, independent information about the depth of the rock slope instability is retrieved by inverting the dispersion curves.

The fundamental-mode resonance frequency is generally related to the depth (Burjánek *et al.* 2010b) or volume of the instability (Burjánek *et al.* 2012). In particular, it has been observed at a number of sites that the fundamental frequency is the same for all stations on the instability. This can be related either to a 2-D/3-D resonance of the unstable rock mass, or to a constant depth of the most significant shear wave velocity contrast. Therefore, it might be possible to estimate the volume of the instability from this frequency if the lateral extent is known. The volume estimation based on the seismic response would represent a cheap alternative to existing methods. There are no geodetic or geophysical alternatives except boreholes which are extremely expensive in alpine environments. However, this long-term objective has not been achieved yet. It is therefore crucial to better understand how specific characteristics of the slopes such as activity level, internal structure, topography, morphology and unstable volumes influence the global seismic response of the instability. We will investigate whether it is possible to find a single resonant frequency for deep-seated instabilities with strongly fractured near-surface layers like Cuolm da Vi, and how the superficial fracturing extends at depth.

2 SITE DESCRIPTION OF CUOLM DA VI

The investigated sites are situated on the northern flank of the upper Vorderrheintal in the vicinity of Sedrun (Canton Graubünden, Switzerland). These slopes are two individual trough shoulders of elevations between 2000 and 2500 m above sea level. They are bordered to the south by the deep incision of the Vorderrhein, laterally by deeply incised Quaternary valleys, and to the north by mountain peaks. Both ridges lie in the large-scale tectonic strike direction giving a similar geological and structural setting. Fig. 2 shows a geological map of the study area with the location of the slopes. We first introduce and analyse the site Cuolm da Vi. In chapter 6, we then introduce the site Alp Caschlè and compare the measurements at Alp Caschlè with the measurements at the site Cuolm da Vi.

The Cuolm da Vi instability has a volume of approximately 150 Mm^3, affects an area of about 1.5 km^2 and moves with a mean velocity of 20 cm yr^{-1} (Amann 2005; Amann *et al.* 2006; Hugentobler 2015). A detailed map of the site can be found in Fig. 3 and a geotechnical profile in Fig. 4.

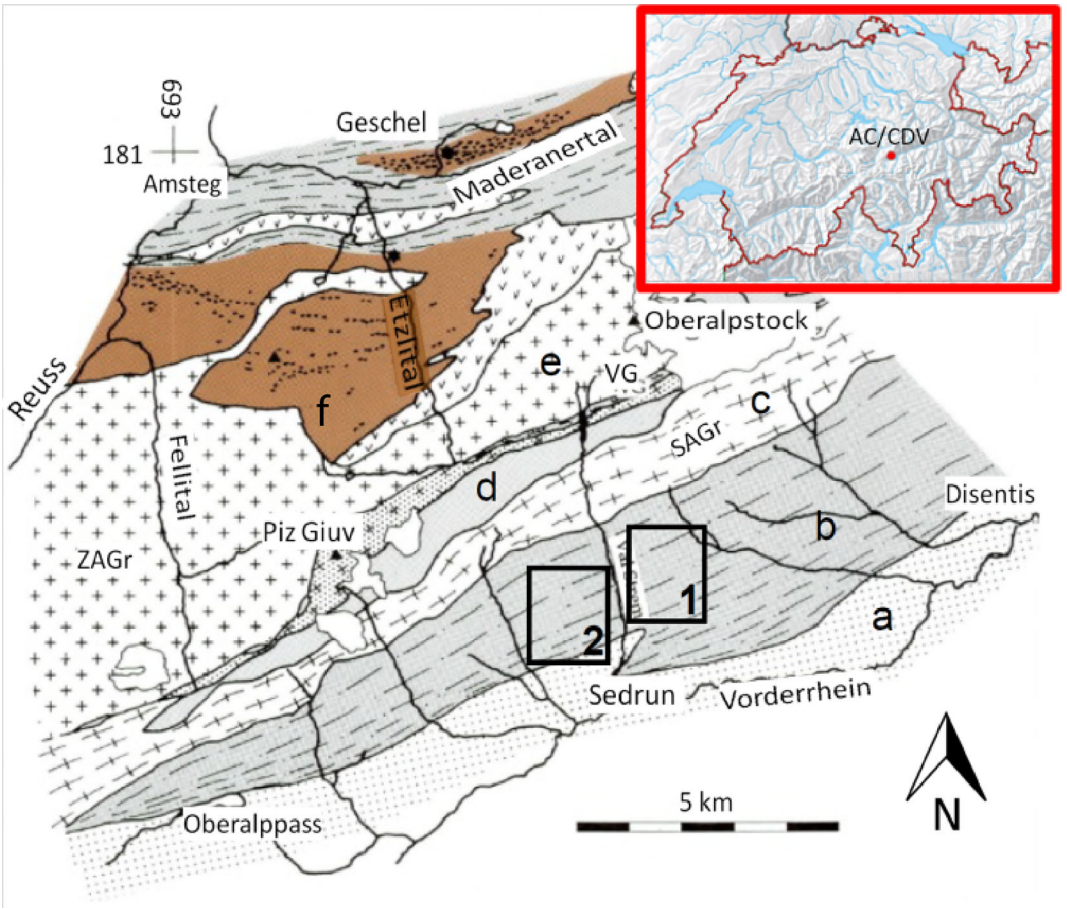

Figure 2. Interpretative petrotectonic map of the eastern Aar massif from Abrecht (1994) with the location of the slopes: 1: Cuolm da Vi and 2: Alp Caschlè. Right upper corner: location of the investigated sites in Switzerland. Units: a: Tavetscher Zwischenmassiv and b: southern Altkristallin. Pre-Variscan gneisses strongly retrograded (biotite-sericite gneisses and schists, biotite-chlorite gneisses and schists and chlorite schists and gneisses); c: southern Aar Granite (lower Carboniferous intrusive); d: pre-Variscan gneisses; e: central Aar Granite (upper Carboniferous intrusive) and f: granitic to tonalitic gneisses.

We find competent gneisses of the southern granite gneiss in the upper part of Cuolm da Vi and less competent gneisses, schists and kakiritic rocks of southern gneiss zone (*cf.* biotite gneiss of the Aar massif south border) in the lower part with respect to the Clavaniev zone (Schneider 1933; Amann 2005). The incompetent kakiritic rock unit that is outcropping in a ravine that forms the SE border of the landslide, is approximately 150 m wide and builds up the toe region of Cuolm da Vi, that is, Drun Tobel. There are two main Alpine foliations (steeply SSE and SSW dipping) and one minor Variscan foliation present. The Alpine foliations are accompanied by persistent fracture systems (joints and faults). Besides fracture systems parallel to the alpine foliation, three other more or less persistent main joint sets can be identified. Uphill and downhill facing scarps which have formed along shear zones are the morphological predominant features in the southern Aar massif and frequently occur at Cuolm da Vi and Alp Caschlè. They typically form stepped reliefs on ridges, as well as depressions along which rock fall and surface water runoff at steep side flanks of the ridges are accentuated (e.g. in Val Strem, between Cuolm da Vi and Alp Caschlè, see Fig. 2). The brittle and ductile shear zones, which have a complex architecture and often a clayey or kataclastic fault core, have lower shear strength than the gneissic host rock. Therefore, the stability is dominated by their occurrence (Amann 2005). Hydrogeological investigations suggest that the unstable rock mass is highly disintegrated. This assessment is based on the observation that within the rock mass area no surface water flow occurs at the western slope towards the N–S striking Val Strem, suggesting a very low water table. This is in contrast to Alp Caschlè, where springs and surface water flow can be observed several hundred metres above the Val Strem valley bottom. In addition to the prominent morphological features which are associated with dislocations along shear zones (uphill facing scarps), there are several instability-related extension phenomena like graben structures, tension cracks and sagging structures (Amann 2005). An overall extensional regime exists at the outer boundary of the deep-seated instability. In Fig. 3, the instability boundary is indicated by a brown dashed line. In the east, it coincides with a major tension crack (red line in Fig. 3) and continues up to Cuolm Parlet dado which is characterized by strong disintegration of the rock mass and double crest formation. The instability stretches over the large graben structure to the west to Cuolm Parlet dadens. That part is characterized by very high displacement rates and a strongly disintegrated rock mass. The rock mass south of Cuolm Parlet dadens shows S-oriented displacements, whereas the rock mass north of Cuolm Parlet tends to move in SW direction due to the reduced lateral confinement and the kinematic freedom towards the western Val Strem (i.e. given by the topography and rock structure orientation). As a consequence of this SW-oriented displacement a large tension crack (close to ambient vibration measurement points 212 and 213) opened in a morphological depression (trough) north of Cuolm Parlet dadens (for a photo,

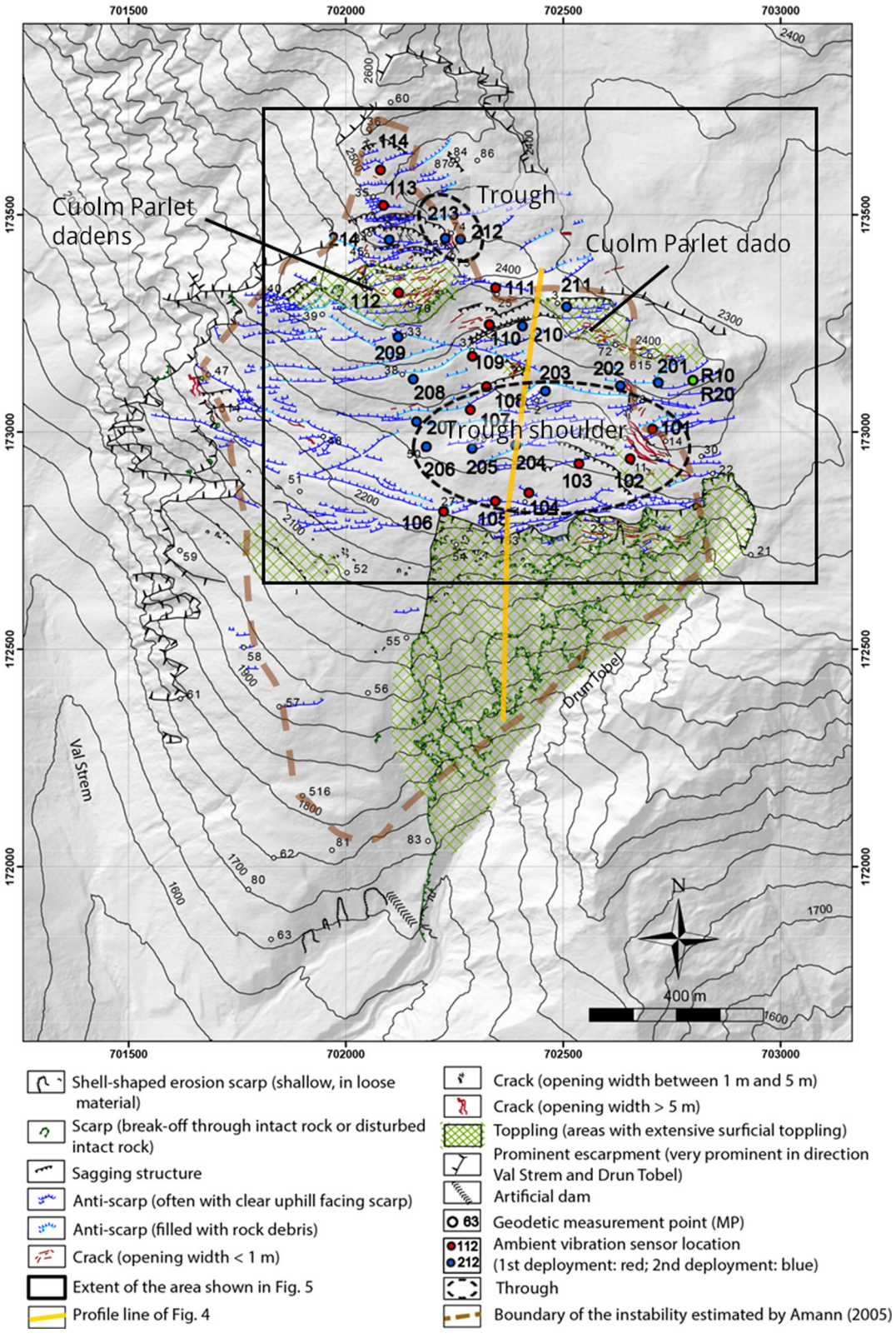

Figure 3. Map of Cuolm da Vi indicating the structures induced by the moving rock slope (modified from Amann 2005 and Hugentobler 2015).

see later Fig. 16, right upper corner). This tension crack is assumed to be the northern border of the instability. The central part of the trough shoulder shows few indicators for very active relative movement (e.g. scarps and antiscarps with small relative dislocation). Toward the Drun Tobel, the number of antiscarps slightly increases. These features are due to local instabilities related to the steep slope at the Drun Tobel.

The recent activity level is demonstrated by absolute displacement measurements. In particular, mean values obtained from Global Positioning System (GPS) measurements between 2005 and

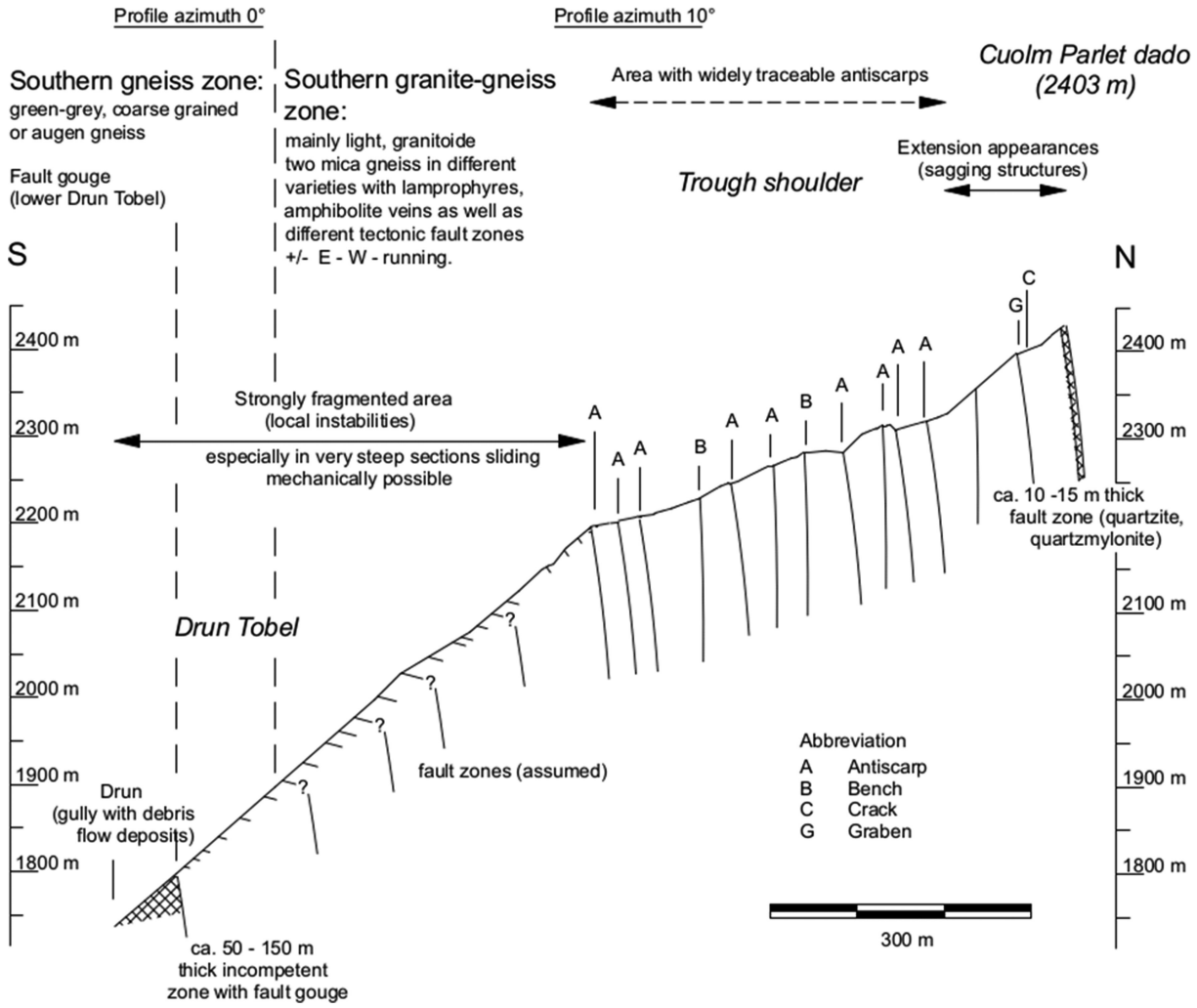

Figure 4. Geotechnical profile of the site Cuolm da Vi (Amann 2005). The location of the profile can be seen in Fig. 3.

2009 have been used (Figs 10 and 12). Comparing the most recent displacement vectors and mean velocities with data from Amann *et al.* (2006), who completed the analysis between 1999 and 2002, no major changes have been observed. Overall, the velocities across the slope show a small decrease compared to earlier measurements. Nevertheless, the mean velocity is still high, between 15 and 20 cm yr^{-1} in the central part of the trough shoulder and up to 40 cm yr^{-1} at Cuolm Parlet dadens. The observed different movement velocities and orientations cannot be explained only by the deep-seated motion of the whole unstable mass, but are interpreted to reflect the superposition of more local, shallow movements on the global deep-seated instability (Amann *et al.* 2006).

3 DESCRIPTION OF THE SEISMIC EXPERIMENT AT CUOLM DA VI

Two sets of instruments were available for the acquisition of ambient vibrations. One set consisted of 12 identical three-component velocimetres with an eigenperiod of 5 s (Lennartz sensor with a Q330 digitizer from Kinemetrics), while the second set of instruments consisted of 3 three-component velocimetres with an eigenperiod of 1 s (Lennartz sensor with a Taurus digitizer from Nanometrics). The second set of the instruments was relatively lightweight, and could be transported just by two persons. In contrary, the first set of instruments allowed for dense array measurements, but was heavy, and required more personnel in the field. The sensors were placed on metal trihedrons, in shallow holes for better coupling with the ground.

At Cuolm da Vi, two array configurations were set up using both sets of instruments simultaneously (15 sensors in total). The configurations are shown in Fig. 3. Instrumental corrections have to be performed before the data processing as different types of instruments were involved. The first array configuration was measuring during the afternoon for about 90 min, while the second configuration was measuring at night for several hours. The noise level during the day is usually higher compared to the one in the night which is due to human activities. A little village and a busy road are located around 2 km away from the instability at an elevation of 1400 m which is around 1000 m lower than the investigated area.

The reference station was supposed to be installed on stable rock. Nevertheless, the borders of the instability were not obvious, neither from orthophotos nor directly in the field. The proposed reference station for the site Cuolm da Vi—R10 which was installed during the first and the second configurations—turns out to show a higher level of ground motions than other stations in the first array and therefore its recordings were found not suitable to be used as reference data during the initial analysis. Consequently, the topmost station, CDV114 was chosen as a reference as it showed

the lowest amplitude in the power spectrum. However, CDV114 was not installed during the second configuration. Therefore, a re-referencing procedure has been applied with the common station CDVR10 (called CDVR20, in case of the second deployment).

The station configuration aimed to cover areas with a variety of morphological features like graben structures, sagging structures and cracks (see Fig. 3) to analyse whether these different features show specific seismic signatures. The high number of simultaneously recording sensors allows using advanced array techniques, but required helicopter transport and 10 persons in the field. In addition, several sensors were installed between widely traceable antiscarps, while a couple of stations were installed in a topographic depression in the central zone of the trough shoulder. The influence on the seismic response of the two major tension cracks in the north and east parts of the landslide is investigated with stations 212 and 213 (in the north) and 101 and 102 (in the east). The stations 103, 104, 105 and 106 were installed in a relatively flat part close to the southern slope.

4 METHODS

4.1 Polarization analysis

The recordings of the seismic ambient vibrations are analysed with the time–frequency polarization analysis (TFPA) proposed by Burjánek *et al.* (2010a). TFPA characterizes the movement of the ground particles for each time step and frequency by an ellipse, which is described by three parameters: the ellipticity, the strike and the dip. The ellipticity is the ratio between the lengths of semi-minor and semi-major axes, and describes the shape of the ellipse. The value of 1 means circular movement, whereas values close to 0 mean linear movement, respectively. Values between 0.3 and 0.4 can be considered as standard for hard-rock sites (Burjánek *et al.* 2014), and could be reproduced in a synthetic test using white noise time-series as input, which represents uncorrelated components of ground motion. The strike gives the orientation of the semi-major axis with respect to north. The dip shows how much the plane of the ellipse is tilted with respect to the horizontal plane. More technical details about the method are described in the papers by Burjánek *et al.* (2010a, 2012). As an example, the output of the polarization analysis for the reference station and a station on the instable part of the slope at the site Cuolm da Vi is shown later in Fig. 14.

4.2 Site-to-reference spectral ratios

The SRSRs of the ambient vibrations are calculated to map the relative amplification of the ground motion across the instability. The recorded time-series are split into non-overlapping time windows (∼100 s). As a next step, for each time window, the Fourier amplitude spectrum is estimated by a multitaper method after Prieto *et al.* (2009) and normalized by the corresponding spectrum of the reference station. Finally, a geometrical mean for all windows is computed. This procedure can be applied systematically in all horizontal directions. Especially, the direction of the main polarization (estimated by TFPA) is of interest as maximum amplifications are usually observed in this direction. The output of the SRSR is a frequency-dependent amplification function of ground motions with respect to the reference station. It can be used to identify fundamental frequencies of the whole instability as well as other resonance frequencies caused by local geological features. A special attention has to be paid to very narrow peaks in the spectra (i.e. harmonic signals), since these are typically related to strong anthropogenic sources like continuously operating machines.

The goal of SRSR is to eliminate source and path specific effects, assuming that sources of the ambient vibrations are far away compared to the aperture of the array. With this assumption only site signatures remain which are related to the instable rock mass. Especially, the amplification factors are considered when judging whether a given rock mass is potentially instable or not with respect to the presumably stable reference site. For amplification factors around 4, we consider rock slopes as significantly weakened (and potentially unstable), while factors 8 or above represent usually heavily disturbed rock associated with unstable slopes. Factors up to 70 have been observed in the entire data set acquired on 25 different rock slopes (Kleinbrod *et al.* 2017). Such extreme amplifications likely result in a slope failure in case of a strong earthquake.

It is assumed that all stations installed within a few hundred metres should record the same ambient-noise wavefield. Ideally, the reference station should have the lowest spectral power, so that a relative de-amplification should not occur within the array in the instable part of the slope. Generally, de-amplification or amplification caused only by geometrical effects (i.e. effects of surface topography) are small with respect to effects caused by the fractured rock (Burjánek *et al.* 2014), and can be neglected. Strong relative de-amplifications across the array are therefore caused by unexpected site effects at the reference station. This is the case for the initially selected rock-reference site at Cuolm da Vi (site R10). A new reference station is then selected as the station with lowest vibration power in the array. A problem arises when such a station is not installed during the entire duration of the experiment (particularly problematic in case of double/triple station measurements). A re-referencing procedure is then necessary, in order to compare two measuring configurations which do not have the same reference station, but at least one common station. In the first step, SRSRs are calculated with respect to the original reference station, which is installed for all array configurations. In the second step, SRSRs are divided with the SRSR of the new reference station, assuming stationarity of SRSR. This means that without any important impact on the environment—as for example, a big rock fall that is changing the volume of the instability—the SRSR is assumed the same, independent of the time of the recording. Re-measurements at other sites have already proven this assumption to be correct (Kleinbrod *et al.* 2016; Burjánek *et al.* 2017).

4.3 Surface wave analysis with the array methods

The vertical components of the array recordings are processed using the HRFK analysis (Capon 1969) using the Geopsy software (Wathelet *et al.* 2008). Such technique allows for the estimation of systematic frequency-dependent time delays in between the array sensors assuming a wavefield consisting of plane waves. These time delays are then related to the dispersion of the Rayleigh surface waves, considering that the vertical component of ambient vibrations is dominated by Rayleigh waves (e.g. Bonnefoy-Claudet *et al.* 2006a,b).

In particular, the recorded time-series are split into non-overlapping time windows. High-resolution beamforming is performed for each time window (Capon 1969), and strongest power maxima are automatically picked in the wavenumber domain for each frequency. Histograms of the picked maxima for each frequency are generated. Finally, the surface wave dispersion curves are selected from visual inspection of the histograms, removal of

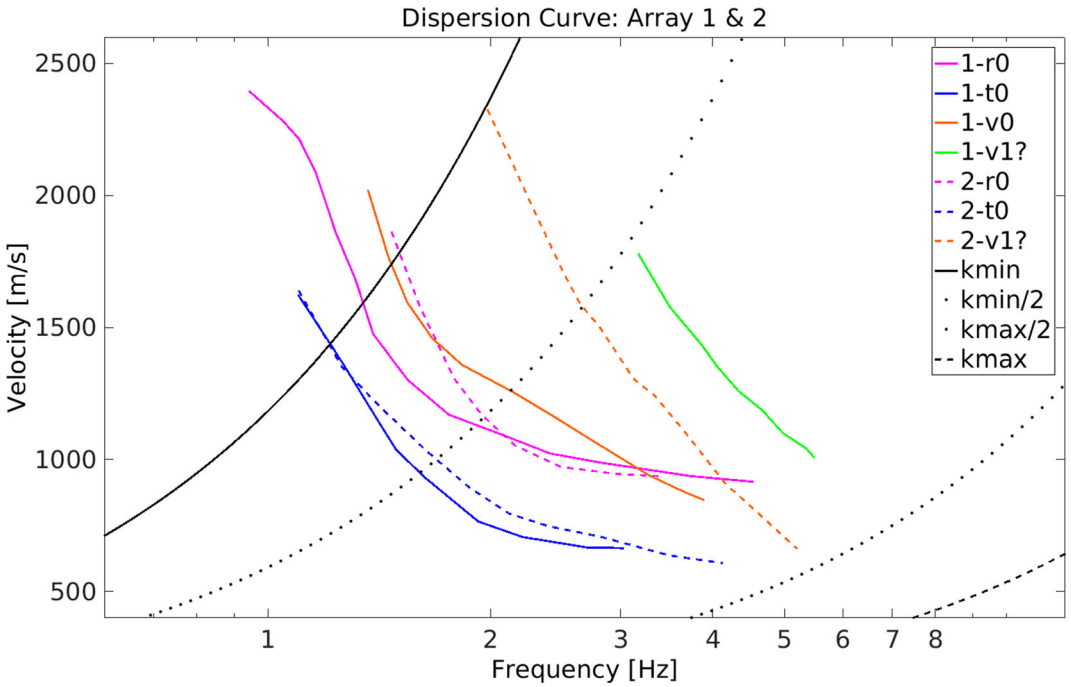

Figure 5. All picked dispersion curves. Solid coloured lines are curves from the first array and dashed lines from the second array. Same colours indicate measurement from the same component. Magenta 1–r0 and 2–r0: fundamental-mode Rayleigh wave obtained from the radial component; blue 1–t0 and 2–t0: fundamental-mode Love wave obtained from the transverse component and orange solid 1–v0: fundamental Rayleigh wave obtained from the vertical component. Orange dashed 2–v1?: first higher mode Rayleigh wave obtained from the vertical component or a mixture of modes; green 1–v1?: first or second higher mode of Rayleigh waves measured on the vertical component. Black lines indicate the resolution limits (solid line: minimum wavenumber k_{min} resolvable by HRFK; dotted line: minimum and maximum wavenumbers resolvable by classical beamforming $k_{min}/2$, $k_{max}/2$ and dashed line: maximum wavenumber kmax resolvable by HRFK).

the outliers and manual picking of the histogram maxima (in the frequency domain).

A similar procedure can be performed for the horizontal components of recorded ground motions (Fäh *et al.* 2008), in order to get the Love-wave dispersion curves. The horizontal components are transformed into radial and transversal components for each assumed direction of propagation in the frequency–wavenumber (FK) domain. The Love dispersion curve can be obtained from the transversal component. The details on the three-component HRFK analysis applied in this study can be found in Poggi & Fäh (2010). Moreover, the ellipticity of Rayleigh waves can be estimated as well, dividing beam powers of the radial and corresponding vertical components (Poggi & Fäh 2010).

In order to get an estimate of the shear wave velocity profile of the site, a combined inversion of the surface wave dispersion and ellipticity curves is performed. The software Dinver is used for the inversion that adopts a modified neighbourhood algorithm (Wathelet 2008).

5 RESULTS FOR CUOLM DA VI SITE

The frequency band of interest extends up to 20 Hz considering the minimum scales (wavelengths) of interest in the order of 10–50 m. This limit originates from our empirical observation at the sites investigated so far that the response usually becomes highly variable for frequencies above 20 Hz for an interstation distance of this order. In general, the data acquisition takes place during dry periods without rainfall. Therefore, the effect of water saturation is mostly neglected in the data interpretation. It is assumed that the water level is low at the investigated sites due to the fast water runoff at rock slopes.

5.1 HRFK analysis and inversion

The data are aquired on an unstable slope containing several open cracks. Surface waves are not expected to propagate beneath compartments that are formed by open fractures, where a normal-mode motion dominates the wavefield (Burjánek *et al.* 2012). Nevertheless, dispersion curves can be retrieved in a limited frequency band between 1 and 5 Hz, with an increase in velocity at lower frequencies. The dispersion curves cannnot be followed for higher frequecnies (>5 Hz) due to the open fractures, so that the *S*-wave velocity of the upper layers cannot be resolved.

The dispersion curves are retrieved for both array configurations and are shown in Fig. 5. All stations are included in the calculation. The aperture of the arrays is almost 1 km, while the interstation distance is around 100 m. Analysing subarrays in similar geological and morphological conditions or excluding single stations does not improve the results. Such step in the analysis simply reduces the size of the array, narrowing the useful frequency band due to the resolution limits of the array. These resolution limits of the arrays are calculated according to Wathelet *et al.* (2008), and the dispersion curves are interpreted only within these limits.

The ambient vibrations of the first array configuration are measured during the afternoon and show a higher level of ambient vibrations than the ones of the second array configuration measuring during the night. Better results (i.e. with fewer outliers in FK plane) are obtained using large time windows, with 300 times the number of wave cycles involved.

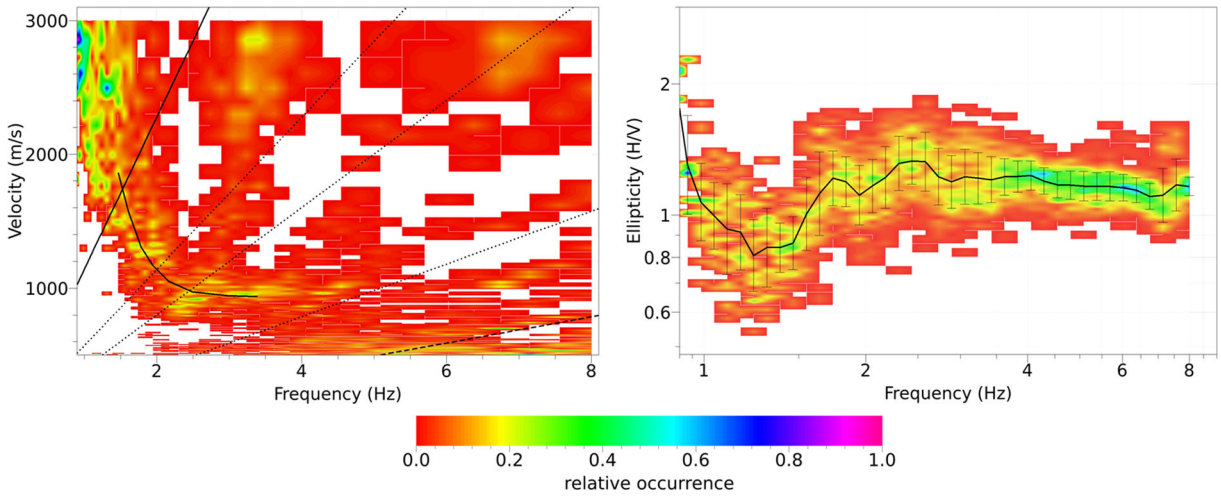

Figure 6. Dispersion curve (left) obtained from the radial component in the second array (curve 2–r0 in Fig. 5), and corresponding ellipticity curve (right).

In Fig. 5, all picked dispersion curves (coloured lines) are plotted together with the resolution limits of the second array (black lines). The solid coloured lines show the results from the first array and the dashed ones from the second array. The transversal (Love waves, 1–t0 and 2–t0) and the radial component (Rayleigh waves, 1–r0 and 2–r0) of both array configurations correspond quite well. They can be tracked between around 1 and 4 Hz, and are addressed as fundamental modes. The velocities lie between 600 and 2400 m s^{-1}. The differences in the observed dispersion curves in the two arrays can be explained by the variability of the internal structure. The arrays are covering different parts of the instability. Therefore, different dispersion curves are expected, representing a mean structure below each array. An example of the dispersion curve picked from the histogram showing the radial component is shown in Fig. 6. The ellipticity curve in Fig. 6 is based on the picked dispersion curve on the radial component, by calculating the radial/vertical ratio at corresponding velocity–frequency points of the dispersion curve (for more details, see Poggi & Fäh 2010). The dispersion curves obtained from the vertical component from the two arrays show some discrepancy. For the first array, two different modes of Rayleigh waves are identified on the vertical component. The first mode (1–v0) is assigned to the fundamental-mode Rayleigh wave dispersion curve, because it is close to the one measured from the radial component (1–r0). The second mode (1–v1) could be the first or second higher mode of Rayleigh waves. For the vertical components, the second array only resolves one mode (2–v1?) with a dispersion curve lying between the two modes of the Rayleigh waves from the first array. This curve might be the first higher mode of Rayleigh waves, or a mixture between the fundamental and first higher mode. This difference in the visibility of modes of the Rayleigh waves that are recorded by the two arrays could be caused by the different noise source distributions. Moreover, the level of the vibrations is significantly lower during the night in the second array configuration.

In a next step, a number of inversions with different setups is performed in order to test different hypotheses for the mode assignment (e.g. with or without higher modes), using variable weights on the ellipticity curve and model space parametrization. Each of these inversion setups delivers slightly different misfits, but the velocity profile does not change much. Finally, 4 out of 10 calculated inversions are considered acceptable, that is, the observed dispersion curves are reasonably well fitted (Figs 7 and 8). Two representative inversions are discussed here, called models 1 and 2, respectively. It is important to note that the plotted misfit values in Figs 7 and 8 are only relative values that depend on the exact setup of the inversion (i.e. ellipticity weight and mode assignment). Therefore, the misfit values between models 1 and 2 cannot be directly compared. The ellipticity curve estimate is subjected to a large uncertainty. In particular, the data basically show that there is not a strong peak in ellipticity, what is still an important constraint for the inversion, although the exact shape is not well constrained. The low weight for the ellipticity is used in order to reject models with large *S*-wave velocity contrasts (i.e. with strong peaks in the ellipticty curve). Nevertheless, the weight used for the ellipticity curve has no major influence on the results of the inversion.

Model 1: this model is based on the dispersion curve for the fundamental Love (2–t0) and fundamental Rayleigh (2–r0) wave, as well as the ellipticity curve with very low weight. The results for model 1 are shown in Fig. 7. The dispersion curves fit well, while the ellipticity does not. In the *Vs*-velocity profiles, there are two interfaces (step-like changes in the *Vs* gradient at depth) visible. One interface is at around 100 m depth, when the *Vs* velocity reaches almost 800 m s^{-1} and then increases to values over 1200 m s^{-1} over a depth range of about 40 m. Another interface is at around 400 m depth, when the *Vs* velocity reaches 1800 m s^{-1} and increases to values over 2400 m s^{-1} over a depth range of about 100 m.

Model 2: this model is based on the fundamental Love (2–t0), fundamental Rayleigh (2–r0) and assuming the curve (2–v1?) as the first higher Rayleigh mode, and the curve (1–v1?) as the second higher Rayleigh mode. The ellipticity of the fundamental Rayleigh mode is also taken into account, with higher weight than for model 1. The results of the inversion are shown in Fig. 8. The fit is variable, with the closest match of the fundamental-mode Rayleigh wave. The inverted velocity models are gradient-type and look similar to model 1. The models obtained with higher weight on the ellipticity and taking into account higher modes are smoother. For model 1, there are two changes in the gradient visible (Fig. 7d) around 100 and 400 m. Model 2 shows—in addition to the interfaces of model 1—a third, very shallow interface at 10 m, while the deepest interface is slightly shifted downwards to around 450 m depth (Fig. 8f). The low velocities below 10 m depth are not resolved by the dispersion curve, and might be an artefact of the inversion. The observation of an interface at around 100 m in both models is within the range of the estimated depth of the instability by Amann (2005), who

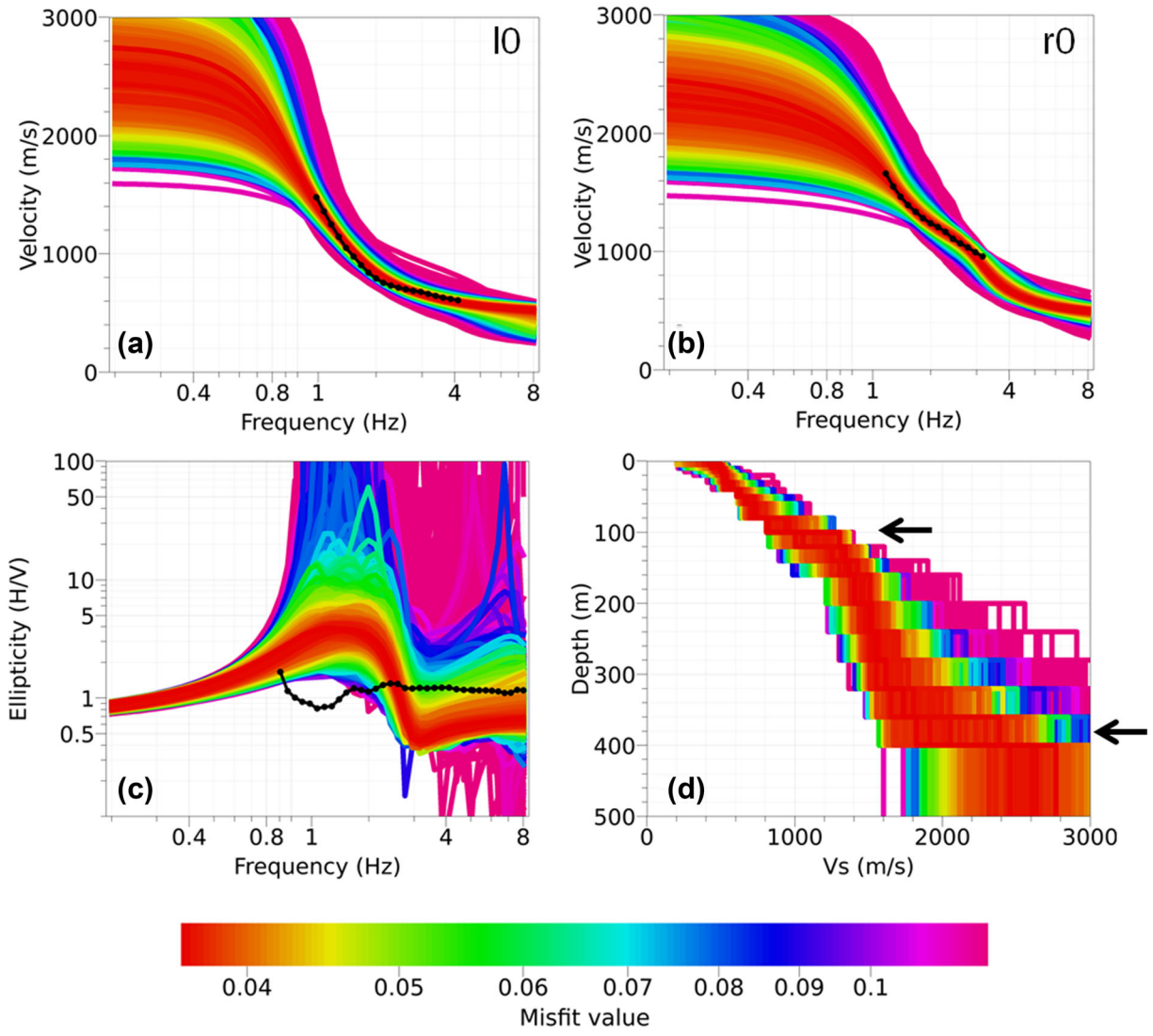

Figure 7. Result of the inversion. Different colours represent different misfit values between the observed (in black) and the modeled dispersion curves during the search. a: 2–t0, b: 2–r0, c: ellipticity and d: resulting *Vs* profiles. Black arrows indicate interfaces in the velocity profile.

combines field observations (in particular, observations along the west slope towards the Val Strem are used for a 3-D interpretation) with numerical modeling results. Amann (2005) finds that the depth of the landslide ranges between 60 and 180 m depending on the location. For the trough region, shear dislocations along faults are estimated to reach a depth of 60–150 m. Superficial disintegration in the area of the Cuolm Parlet dado and dadens are estimated by Amann (2005) to be <15 m, which is consistent with the shallow interface.

Ten representative velocity profiles for four selected inversions are plotted in Fig. 9. This provides an overview of the variability of all inverted velocity profiles. The different velocity profiles are in good agreement, showing a gradual increase of the shear wave velocity with depth. The first 20 m show large scatter as the shallow depths are not constrained by the dispersion curves retrieved from this measurement. First, the minimum interstation distance is too large to capture the high-frequency part of the dispersion curves. Second, the structure is likely very heterogeneous in the first 20 m, so the assumption of a 1-D layered structure might be invalid. This gradient-type velocity structure indicates gradually increased disintegration of the rock mass close to the surface. At around 100 m depth, a clear change on the *S*-wave velocity gradient is evident, which might indicate the depth of the instability as proposed by Amann (2005). Amann (2005) showed field observations and displacement measurements, which provide complementary information to the ambient vibration analysis. The different parts of the instability show different activity levels. Areas with larger displacements are often more fractured than less active areas. We therefore would expect the more active part with more fractured material to show higher amplification factors. However, this does not imply that non-active rock slopes do not show amplification, because present activity might not represent the activity of the past. Fig. 10 shows all measuring points with displacements (black arrows), the two main tension cracks (red bars) and four coloured areas representing separately analysed subarrays. The displacements around the stations 112, 208 and 209 are much larger than in the area around the stations R10, 201 and 202. Based on the results of the ambient vibration analysis of the single-station recordings, we divide the area into different subareas or subarrays. This will be discussed in detail in the following section.

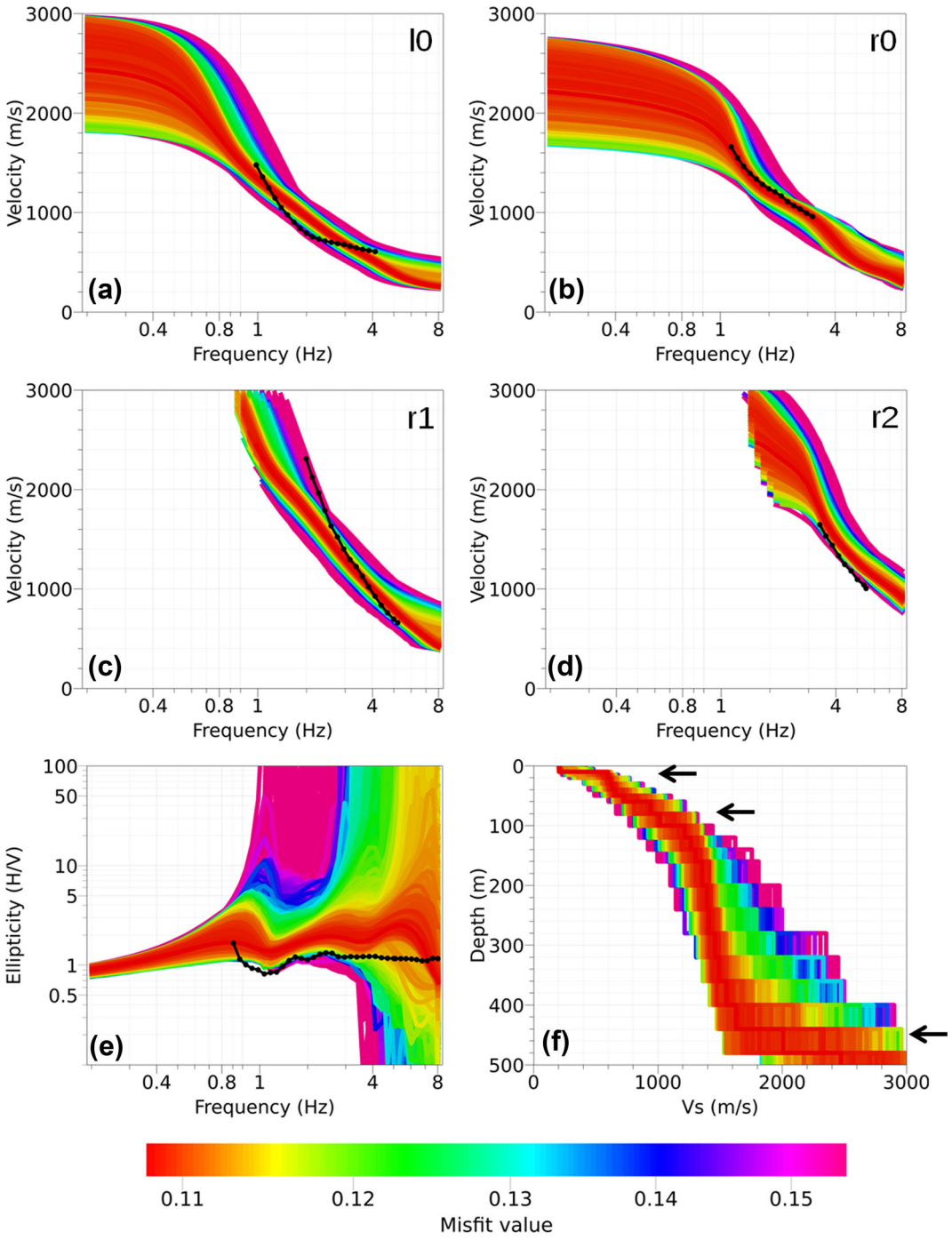

Figure 8. Different colours represent different misfit values between the observed (in black) and the modeled dispersion curves. a: 2–t0 assumed to be the fundamental-mode Love wave; b: 2–r0 assumed as fundamental-mode Rayleigh wave; c: 2–v1? assumed as first higher mode Rayleigh wave; d: 1–v1? assumed to be second higher mode Rayleigh wave; e: ellipticity curve and f: derived *Vs* profiles. Black arrows indicate interfaces in the velocity profile.

5.2 Site-to-reference-spectral ratios and polarization analysis

SRSRs are calculated for 2 hr of ambient vibration recordings for all stations and both array configurations. Station CDV114 is used as a reference station. In Fig. 11, the SRSR curves for three different directions (north, east and vertical) and of the geometrical mean of the two horizontals are plotted for the two stations CDV101 and CDV112. The low-frequency part (up to 5 Hz) shows a linear trend for all stations. This feature is linked to the characteristics of the deeper underground at the site Cuolm da Vi characterized by the *Vs*-velocity gradient. In the higher frequency range, the seismic response starts to vary from station to station. The high-frequency (>10 Hz) response is related to small-scale geological features within the instability and might also be strongly affected by the presence of local anthropogenic noise sources (e.g. the cable car close by). Considering the frequency range above 10 Hz, and the seismic velocities obtained in the previous section, the response above 10 Hz represents mainly shallow features (down to a depth of around 20 m). In general, high-frequency response shows stronger

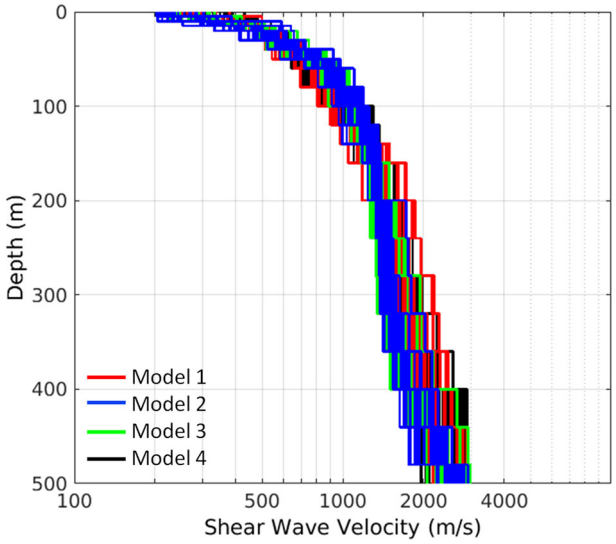

Figure 9. Variability of 10 chosen velocity profiles from each inversion using four selected input models. Each colour represents a different input model.

variability in time and space, stronger directionality and higher levels of amplification than low-frequency response. The limited spatial density of arrays does not allow for meaningful mapping at this frequency range (>10 Hz). Therefore, the focus lies on the frequency band from 1 to 10 Hz. Moreover, the reference station CDV114 is affected by strong local effects above 10 Hz. Consequently, all figures only show the frequency band up to 10 Hz.

In general, SRSR show spatial variations across the site Cuolm da Vi with a complex pattern. This makes it difficult to compare and interpret the recordings of all stations together. In order to simplify the interpretation of the data, the compartments on the unstable area are subdivided into smaller subarrays for which we clearly see common features in the frequency range 3–10 Hz. Fig. 10 shows the four differently coloured areas representing the separately analysed subarrays. The subdivision is mainly based on the amplification results. For frequencies below 3 Hz—representing the deep (>150 m) and intermediate (35–150 m) structure—the seismic response for all stations is similar. The difference between the sensor's SRSR amplification gets evident, when comparing SRSR for 3 and 8 Hz (Fig. 12). Cold colours (blue–green) indicate low amplification and warm ones (orange–red) high amplification. It gets obvious that the region around station 107 and 109 shows only little amplification (subarray C as defined in Fig. 10 in orange). The horizontal profile (subarray B in Fig. 10 in green) formed by 102, 103, 104, 105 and 106 contains as well low amplifications. For the upper part of the instability (subarray D in Fig. 10 in red), including 113, 212, 213 and 214, the displacements and geological properties are different compared to the rest and forms an additional subarray. Independent movement from the main mass, southwest oriented displacements due to reduced lateral confinement in the west and the kinematic freedom caused by the south moving main mass as well as very active subparallel tension cracks with secondary

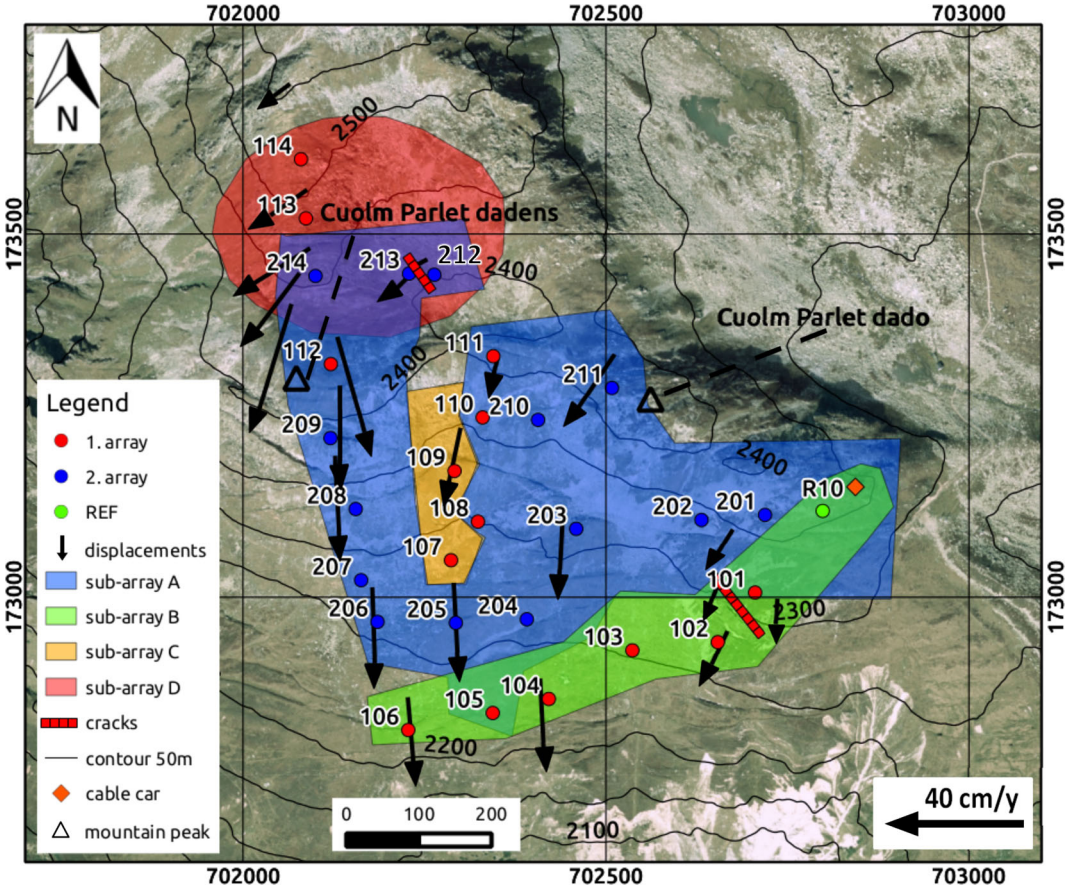

Figure 10. Overview of the measuring configuration. R10 is installed during both array measurements. The black arrows illustrate displacements measured with differential GPS between 2005 and 2009 by Donatsch Ingenieure AG. The coloured areas represent the separately analysed subarrays. The separation of the different areas is based on the analysis of the ambient vibration recordings. The properties of the observed dynamic response are discussed in Table 1.

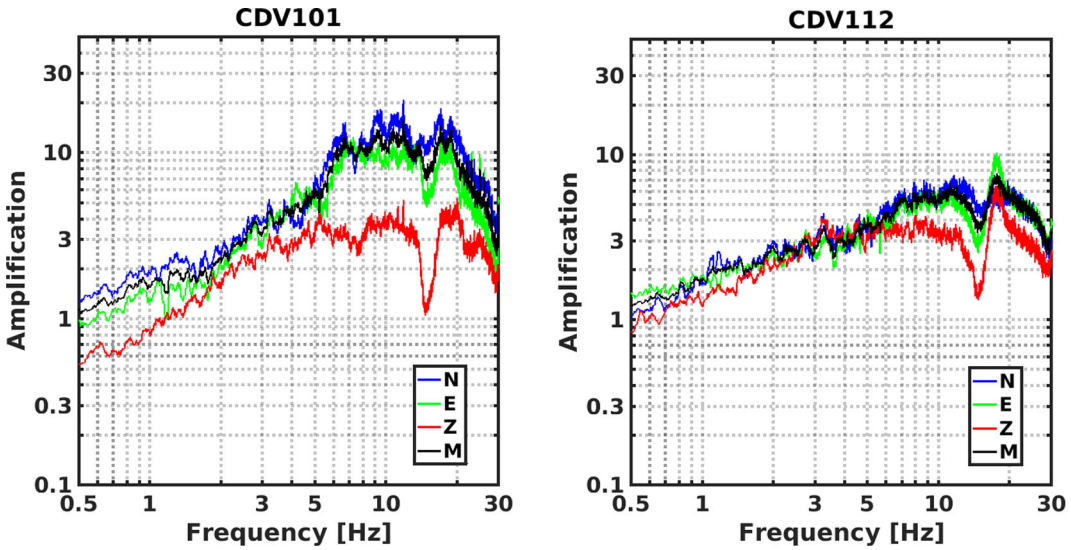

Figure 11. SRSR curves for north, east and vertical components as well as for the geometrical mean of the two horizontal components for the stations CDV101 and CDV112. The reference site is CDV114. At lower frequencies (<5 Hz), the curves for the two sites look similar, whereas at higher frequencies differences are larger.

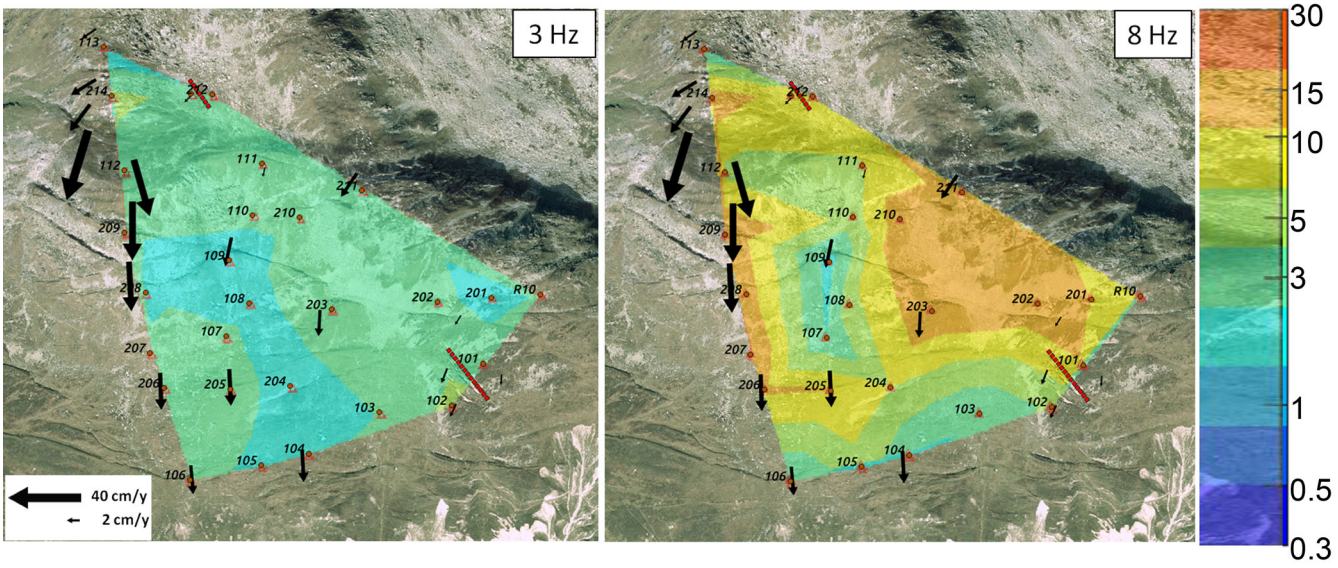

Figure 12. SRSR map for 3 Hz (left) and 8 Hz (right) measured at Cuolm da Vi showing the amplification. The activity is defined by the velocity vectors (black arrows) calculated from differential GPS measurements (monitored between 2005 and 2009) provided by Donatsch Ingenieure AG. The vectors show the orientation and magnitude of the movement velocity at the GPS points. The red dashed bars between the stations 101 and 102, respectively, between 212 and 213 indicate the main cracks.

sagging rock blocks are observed in subarray D (Hugentobler 2015). The biggest subarray A includes the whole area without the just mentioned upper part (subarray D) and the low-amplification spots in the mentioned profile (subarray B). The stations from subarray A are situated in the blue area in Fig. 10, and contain a characteristic trend in their SRSR between 3 and 10 Hz (Fig. 13a). The subarrays A–D mapped in Fig. 10 are briefly described in Table 1.

The results of the polarization analysis (Figs A1 and A2 in Appendix) only show one common polarized feature at around 1.1 Hz which is likely related to a dominant anthropogenic source and not to the instable rock mass at Cuolm da Vi. There are no further common patterns recognizable. A few stations show weak polarization in variable directions at different frequencies which is most likely due to very local features. The only significant features that can be observed, is a polarization for stations located close to the observed open cracks, with a polarization in the direction perpendicular to the crack (CVD 102 in Fig. 14, and in map representation in Fig. 15). There is no visible polarization at station CDV114, which is used as reference (Fig. 14).

Subarray A (blue colour in Fig. 10 and Table 1): the stations belonging to this subarray have one significant feature in common. Between 3 and 10 Hz, they all show a trend in their SRSR which is raising with increasing frequency (Fig. 13a). The geographical locations of these stations are distributed over the whole unstable area. This trend seems to be a feature caused by the *Vs* gradient in the upper 35 m, and is very stable in space and time. In particular, this estimate is supported by measurements of the surface wave dispersion curves and the results of their inversion (shear wave velocity of 500–700 m s^{-1} at 50 m depth). The smooth gradient *Vs* profiles result in rather smooth amplification functions typical for the

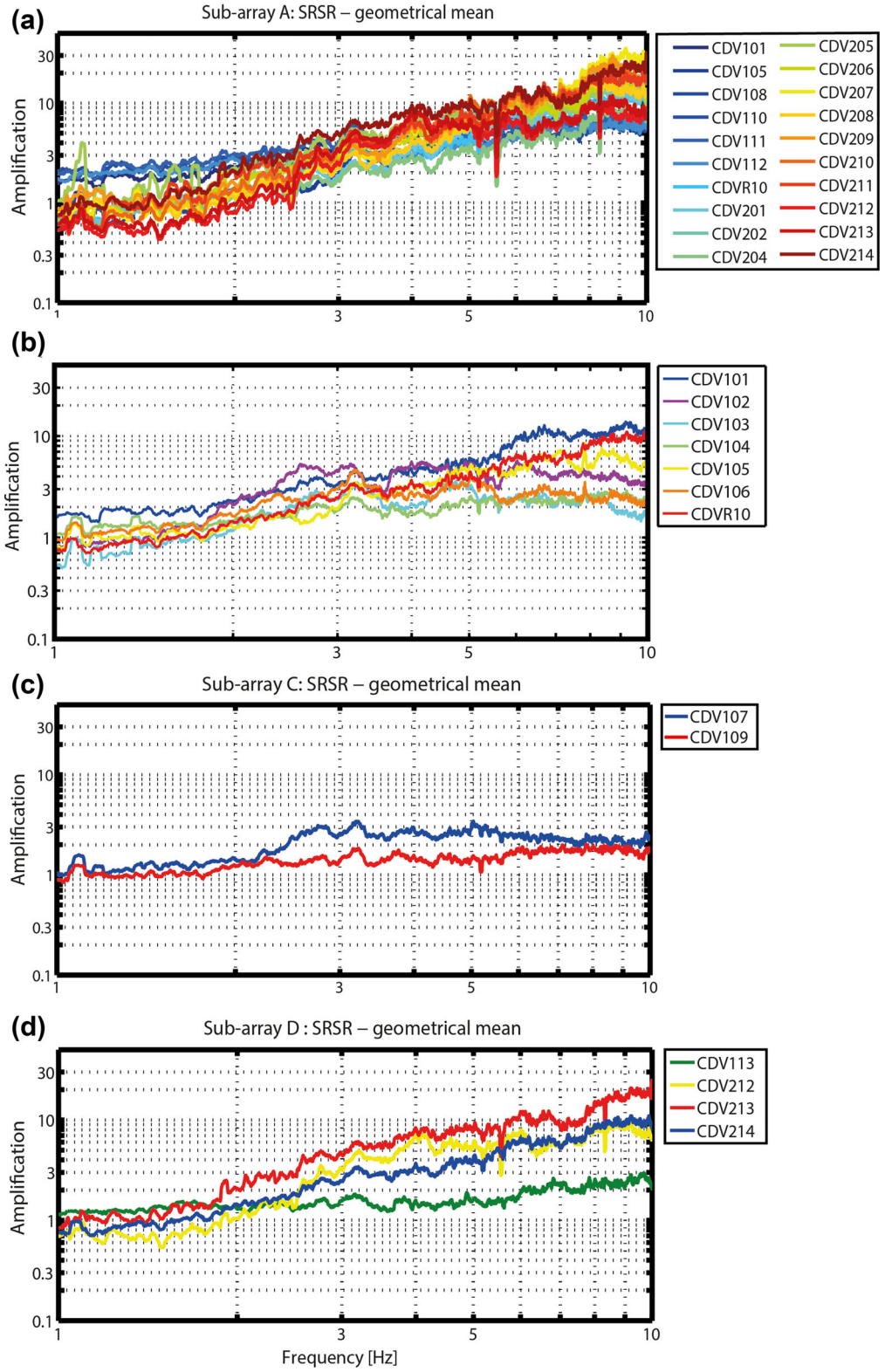

Figure 13. (a) Subarray A: SRSR curves showing a linear trend from 3 to 10 Hz for all station (blue area in Fig. 10); (b) subarray B: SRSR curves are more scattered at higher frequencies (green area in Fig. 10); (c) subarray C: CDV107 and CDV109 show very low amplification (orange area in Fig. 10); (d) subarray D: SRSR curves of the 'northwest break-off' (red area in Fig. 10).

rock sites (Poggi *et al.* 2011). In contrast, the seismic response for frequencies around 10 Hz shows more variability between the stations and is assumed to represent the local and partly disintegrated, shallow underground down to 10 m, which is very complex at Cuolm da Vi. For frequencies above 7 Hz, the stations show amplifications from 6 up to 20. The results of the polarization analysis do not show any common feature for this subarray. Most of the stations seem to show weak polarization in variable directions and

Table 1. Subarrays defined for Cuolm da Vi. A map with the subarrays is shown in Fig. 10.

Subarray	Stations	Features/characteristics/amplification
A	101, 105, 108, 110, 111, 112, R10, 201, 202, 204, 205, 206, 207, 208, 209, 210, 211, 212, 213, 214	A trend in SRSR from 3 to 10 Hz: (a) All the stations show a trend in the SRSR curves with increasing amplification to higher frequencies (b) Trend most likely related to the measured *Vs*-gradient down to 35 m depth
B	102, 103, 104, 105, 106, (101, R10)	Horizontal profile: (a) Flat amplification between 3 and 5 Hz (b) West from the crack (102 and 103) velocity vector small; 102 shows strong polarization (c) Eastwards high amplification above 5 Hz and polarization close to crack (101 and R10)
C	107, 109	Located in a depression: (a) Low amplification that is flat between 3 and 10 Hz
D	113, 212, 213, 214	Upper part of the instability: (a) Different geodetic/geological properties (independent from main mass, southwest oriented displacements, active subparallel tension cracks with secondary sagging rock blocks (b) Polarization around the crack

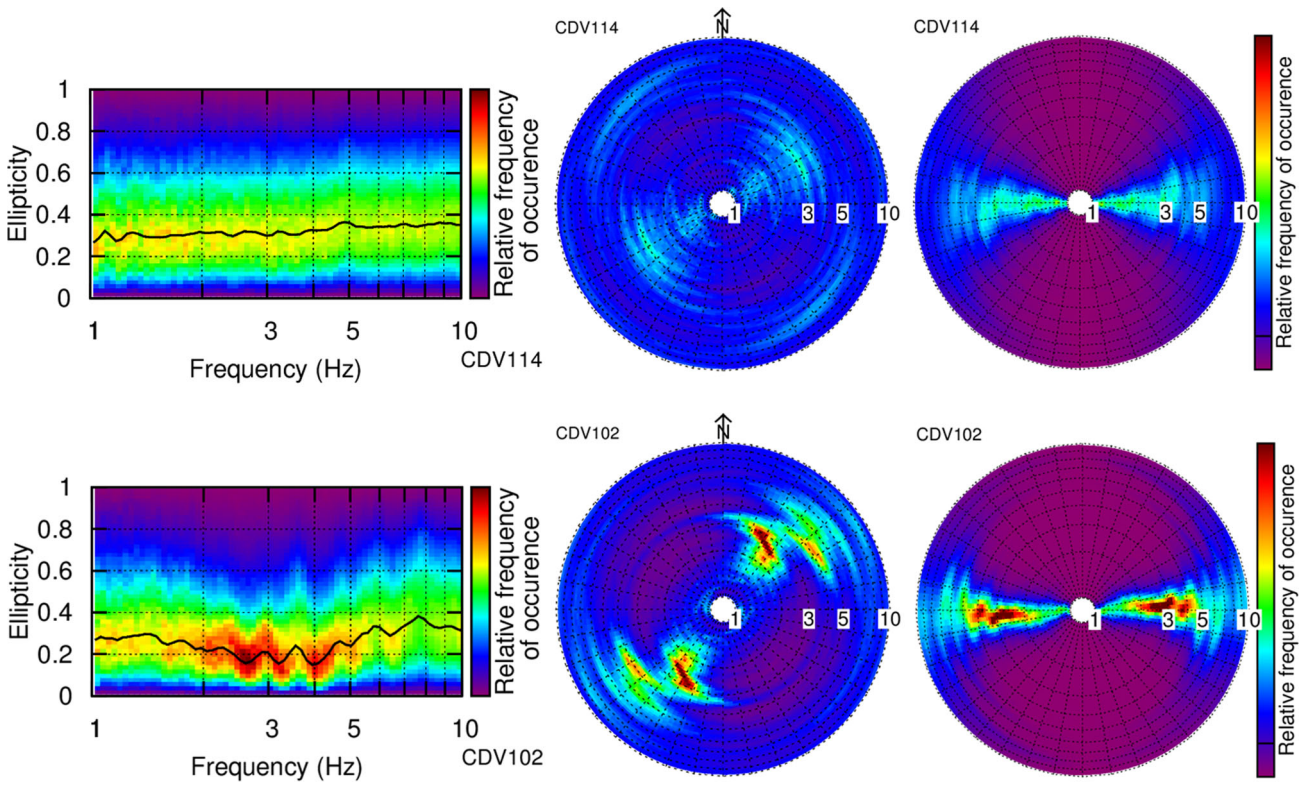

Figure 14. Output of polarization analysis. Top: results for the reference station of the first array at Cuolm da Vi (CDV114). The colour tells how often a certain frequency occurs in the ambient vibration recording (red = often and purple = seldom). Top, left: ellipticity plot indicating an intact rock site. Top, middle: strike plot—north direction goes from the circle centre vertically up, the radius represents the frequency in Hz. There is no clear polarization visible except a very weak one at 3 Hz with an azimuth of around 60°. Top, right: dip plot—no significant features visible. Bottom: results for station CDV102 on the instability (close to a tension crack). It shows clear polarization features at 2–3 and 5 Hz with an azimuth of 30° and 55°, respectively. The dip of about 5° shows that the ellipse formed by the ground motion is slightly tilted towards the horizontal plane at the surface in the frequency band around 2–3 Hz where the ground motion is directional.

frequency bands, which is most likely related to very local geological features (e.g. single blocks, open cracks, etc.). Polarization plots for all stations are given in the electronic Appendix.

Subarray B (green colour in Fig. 10 and Table 1): these stations are grouped on the southern horizontal profile including the stations 102, 103, 104, 105 and 106. The stations 101 and R10 actually belong also to subarray A, but for comparison they are plotted in the figure for subarray B as well (Fig. 13b). Up to 5 Hz, the curves look similar, with a flatter gradient in the SRSR between 3 and 5 Hz. For frequencies above 5 Hz, the SRSR start to differ more, and—depending on the site—show amplifications in the range of 2–10. Between the stations 101 and 102, there is a 5–10 m wide tension crack running from northwest to southeast (see Fig. 15) causing an clear change in the seismic response of the stations

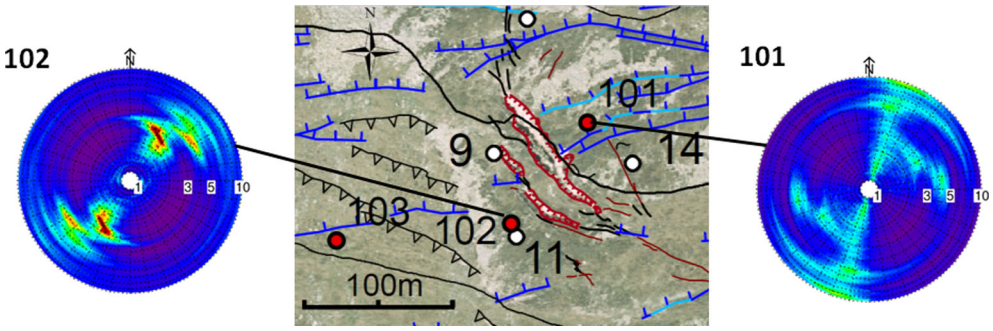

Figure 15. Detailed orthophoto showing the main crack with an opening width >5 m (thick red lines) and the nearby stations 101 and 102 (red dots) with their strike plots indicating the polarization of the ground motion. The thin red lines show smaller cracks (opening width <1 m). The white points are the GPS locations (9, 11 and 14) with velocity vectors of 1.5 (14), 3.6 (11) and 4.5 (9) cm yr^{-1}. The dark and light blue lines represent antiscarps, whereas the light blue ones are filled with debris. The black lines with triangles indicate sagging structures, short black lines without triangles point out cracks with an opening width between 1 and 5 m, while long black lines without triangles show the height lines.

east- and westwards from the tension crack. The stations 101 and R10 are located eastwards from the tension crack and for frequencies above 6 Hz, they show amplification factors between 5 and 10, whereas the stations westwards from the crack (103, 104 and 106) show low amplifications of two or three over a broad frequency band from 3 to 10 Hz. In contrast, station 105—the second most western station of the horizontal profile—shows higher amplifications of 5–6 above 5 Hz that likely represents a subsite with a larger disintegration of the rock close to the surface. The SRSR of station 102 are similar to the ones at 103, 104 and 106, but slightly more amplified, most likely caused by its closeness to the open tension crack at the eastern boundary of the landslide. The crack separates the western part (102, 103, 104, 105 and 106) from the eastern part with higher amplifications. The stations which are closest to the crack (101 and 102) show as well the polarization in the direction perpendicular to the open tension crack. The polarization of station 102 that is located westwards from the crack is much stronger compared to the one of station 101 (Fig. 15). This is plausible as 102 is located on an area restricted by the crack and a cliff in the south. Therefore, the freedom of movement is considered to be higher than in the area, where 101 is installed with constraining rock in the north. The maximum polarization at site 102 is around 2.5 Hz, indicating that the tension crack is deep (tenths of metres, considering the velocity profile obtained from the inversion). This strong polarization can be explained by the fact, that through the open tension crack the rock mass westwards gets detached from the rest of the rock slope and the blocks have a higher freedom of movement. Furthermore, the polarization between 3 and 5 Hz is slightly rotating from station 101 to 102. Assuming the measured velocity profiles to be valid at the site 102, we can estimate the depth of the crack from the quarter-wavelength representation of the profiles (Joyner *et al.* 1981; Poggi *et al.* 2011), so that the depth corresponds to the profile's quarter-wavelength depth at the frequency of 2.5 Hz, which is between 43 and 49 m. This estimate defines a lower bound of the crack depth, because the velocities in the area of subarray B are probably higher due to reduced disintegration of the rock material, as it will be explained in the following.

We might interpret the observed flat amplification between 2.5 and 5 Hz in the western part of subarray B as an indication that at a depth between 15 and 50 m, the disintegration of rock is not present as it is in subarray A. This means that this part of the instability can be considered as separated blocks (in particular 102 on a block separated from 103 and 104 on another block), detached evidently between sites 101 and 102 by the deep open crack. Sites 101 and R10 are obviously on a separated block. The detachment from the upper part of the instability as well as the exact subdivision of the blocks remain unclear. Another indication of such separation of blocks might be the amplification between 5 and 10 Hz, which is determined by the level of disintegration of the rock in the shallow part at the specific site. In particular, the sites 103 and 104 show no increased amplification between 5 and 10 Hz, similar to the amplification between 2.5 and 3 Hz. The same is true for site 102, only that the level of amplification is slighlty higher. Also note that the velocity vector measured from GPS close to site 102 is very small.

Subarray C (orange colour in Fig. 10 and Table 1): the amplification for stations 107 and 109 between 3 and 10 Hz is flat and small (Fig. 13c). At site 109, there is a GPS measuring point showing an average displacement rate of 13 cm yr^{-1} in the direction of 192° from north (measurement from 2009). The closest measuring point to 107 is around 100 m southwards showing a displacement rate of 17.4 cm yr^{-1} in the direction of 177° from north (measurement from 2005). Two other points in the vicinity east- and southwestwards from 107 show similar displacements with north–south trend. The response of the two stations is very close to the reference conditions CDV114, which is considered as a stable part of the slope, as their SRSRs are mainly between 1 and 3. Considering the terrain and the topography around these measuring points it gets obvious that the two stations are installed in a north–south running depression. The stations eastwards on the ridge are clearly higher amplified indicating that the ridge material is not intact but fractured. The interpretation for the sites 107 and 109 is difficult. Relying on the interpretation for the sites in subarray B, one might argue that a graben structure was formed in the past, with a block structure inside the graben. Due to the presence of the depression, we might speculate that the weathered surface material has been eroded.

Subarray D—northwest break-off (red colour in Fig. 10 and Table 1): according to displacement measurements and field investigations, the northwest slope of the instability Cuolm da Vi—including the stations 113, 212, 213 and 214—is behaving differently to the main unstable rock mass. With the exception of station 113, all stations show a trend in their SRSR between 3 and 10 Hz, similar to the sites in subarray A, with amplifications of factor 8 or higher between 8 and 10 Hz (Fig. 13d). This indicates a similar disintegration of the rock down to a depth of around 40 m. The station 113 that is installed very close to the reference station 114 shows low amplifications with factors smaller than 3 and therefore

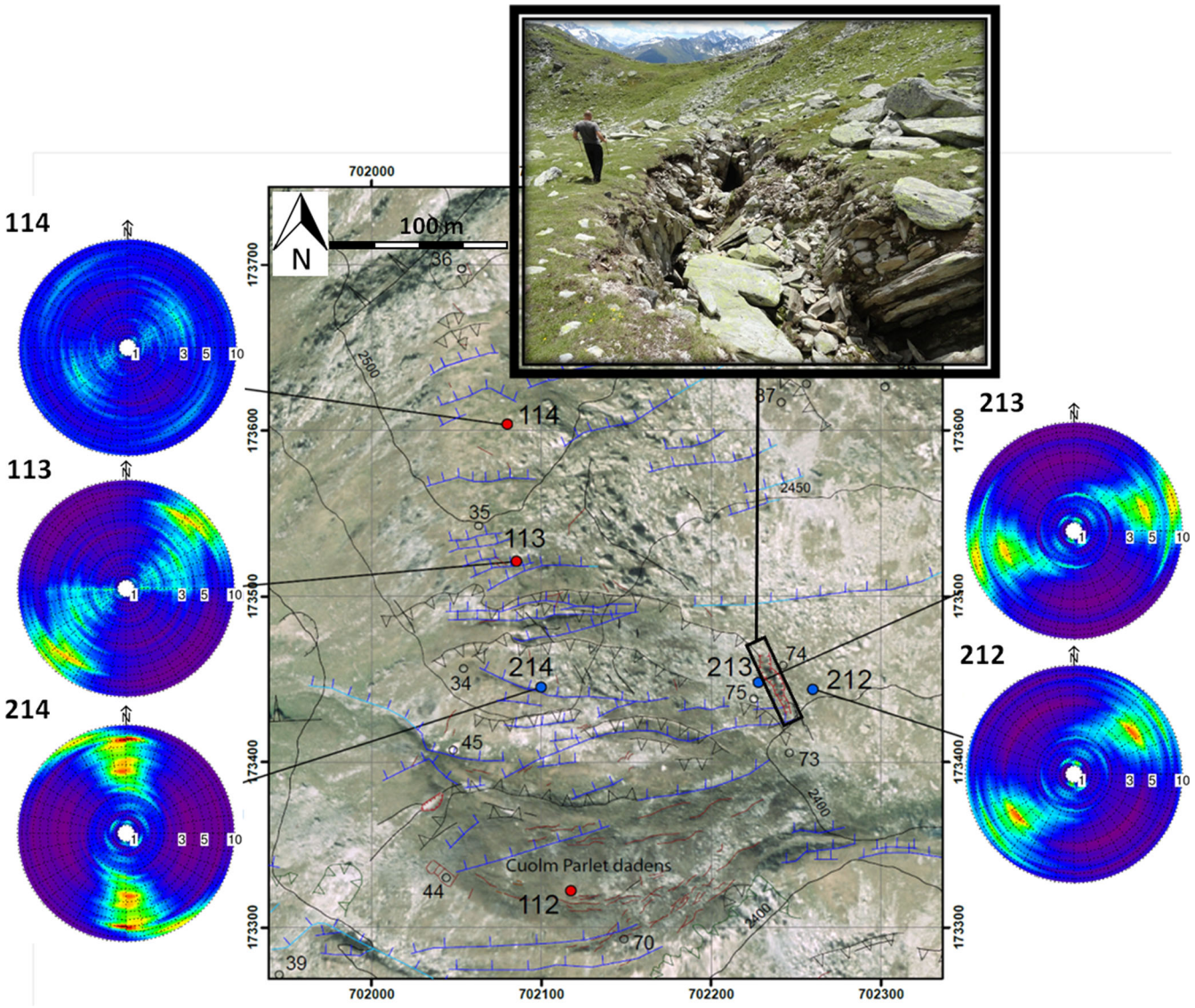

Figure 16. Polarization of the ground motion. Red and blue dots show the measuring locations. For the stations 113, 114, 212, 213 and 214, the strike plot is shown as well. Red thin lines indicate cracks. One of the main cracks is located between station 212 and 213 surrounded by a black box. A detailed photo of this tension crack in the northwest break-off is shown in the right upper corner. The dark and light blue lines represent antiscarps, whereas the light blue ones are filled with debris. The black lines with triangles indicate sagging structures, while long black lines without triangles show the height lines.

it represents a relatively stable part. The stations 212 and 213 are located on either side of the main tension crack in the depression north of Cuolm Parlet dadens and show a strong polarization perpendicular to the strike of the main tension crack at a frequency of about 4.3 Hz.

Fig. 16 shows the map of this subsite with the outcomes of the azimuth versus frequency polarization analysis of the individual sensor locations. The whole ridge north of Cuolm Parlet dadens experiences an outward rotation towards west along a steeply dipping, persistent joint set which is striking SSE. Deep secondary sagging movement occurs only in the southern part of the ridge (around sensor location CDV214) evidenced by several subparallel scarps. The rock mass within this secondary sagging structure is strongly disturbed.

Fig. 16 shows that station 114 (the reference station) shows hardly any polarization, whereas the other four stations show polarized particle motion. The stations 113, 213 and 212 have polarization directions striking between 230° and 250°. This is approximately parallel to the observed movement direction and perpendicular to the most active tension cracks in the region striking approximately SSE. Only the location CDV214 is polarized in the N–S direction (i.e. normal to the scarp in close vicinity of the station). At this location, the steeply south-dipping shear zones—along which the sagging occurs—obviously cause main stiffness anisotropy with a higher compliance in N–S direction.

The large tension crack in subarray D is an important active feature (see Fig. 16, right upper corner). The width and length of this crack have increased dramatically in the last 10 yr (Amann 2005, personal communication, 2016). It can be followed for approximately 60 m along its strike and has a maximum width of over 5 m. The opening direction of this tension crack is approximately 240° causing strong polarization at the nearby stations 212 and 213. The exact depth is still unknown due to the rock debris infill in the crack, but from geological considerations, it constitutes at least 15 m. The

depth can be estimated from the measured frequency of 4.3 Hz at which polarization occurs. Assuming the measured velocity profiles to be valid close to the crack, we can estimate the depth of the crack from the quarter-wavelength representation of the profiles, so that the depth corresponds to the profile's quarter-wavelength depth at the frequency of 4.3 Hz, which is between 18 and 22 m.

6 ALP CASCHLÈ

This site is geologically, structurally and morphologically very similar to Cuolm da Vi. A detailed map of the site is shown in Fig. 17 and a geotechnical profile in Fig. 18. Alp Caschlè has an erosional caldera in the southern part of the slope which, however, shows a much lower activity in terms of rockfall events as compared to the Drun Tobel at Cuolm da Vi. The steep lying rock fabric (initially steeply dipping in direction SSE) shows an extensive disintegration and an overturning to NNW-dipping of rock segments at the trough shoulder and the steeper south slope of Alp Caschlè. Antiscarps are traceable over long distances (several 100 m) and can directly be related to shear zones. The main shear-zone orientations strike E to ENE and dip steeply in direction south and less frequently steeply north (Frei & Löw 2001), which is similar as on Cuolm da Vi. The geology of the trough shoulder is also built up by the southern granite gneiss followed by the biotite gneisses of the Aare Massif south border and the Clavaniev zone outcropping at the erosional caldera L'Ondadusa (*cf.* Geological map by Frei & Löw 2001). Displacement measurements show very little activity for this slope (Amann 2005, and references therein). The explanation for the lower activity at Alp Caschlè might be associated with the thickness of the weak kakirite zone at the toe of the slope (Amann 2005). Amann (2005) showed that the weak kakirite at Cuolm Da Vi is several decametres thick and controls the stability of the entire rock slope. At Alp Caschlè, the thickness of this kakirite zone is significantly smaller. Furthermore, geodetic deformation measurements, performed within the Gotthard base tunnel investigations, reveal a possible, very slow uplift ($\sim$0.3 mm yr^{-1}) of the south part of the trough shoulder relative to the more northern part. Dislocations occur primarily along the pre-existing steep lying shear zones (Frei & Löw 2001). This relative displacement is, however, measured across fault zones at the valley bottom of Val Mila and it is assumed that the sometimes up to several metre high antiscarps at the trough shoulder of Alp Caschlè have accumulated their relative displacement over centuries, mainly by deep-seated gravitational slope deformation. Nevertheless, postglacial uplift, as suggested by Ustaszewski *et al.* (2008), could be an alternative explanation.

Fig. 18 shows a cross-section through the instability. The location of the profile is given in Fig. 17. At the site Alp Caschlè only, the second set of instruments (three sensors) is used, so that triple station measurements are performed. Thus, the data aquisition is not performed simultaneously at all points of interest. One station is kept at the reference point, while the other two stations are moved from point to point. The limited number of simultaneously recording stations does not allow calculating dispersion curves. The interstation distance lies between 100 and 200 m. Each measurement lasts 90 min. Here, the goal was as well to capture the influence of the various morphological features on the ground motion. Referring to Fig. 17, AC1 was installed south of a sagging structure and AC2 north. AC3, AC4, AC6, AC7, AC8 and AC9 were installed in a region of several antiscarps, AC5 was located in the west and outside the antiscarp area. AC10, AC11, AC12 and ACR1 (the reference site) were installed northwards of the antiscarps in a topographic depression which is a very prominent feature at Alp Caschlè. Similarly as at Cuolm da Vi, the original planned reference station is found to be amplified with respect to the other stations. Finally, AC9 is chosen as the new reference station and a re-referencing has to be done.

The polarization analysis (Fig. A3) does not show any common features for the site. Most of the stations show hardly any directionality. Stations AC3, AC4 and AC7 show only light polarization striking approximately west and two stations AC1 (at 5–18 Hz) and ACR1 (at 1–20 Hz) show a clear south-striking polarization (Fig. A3). While looking at the SRSR (Fig. 19), it gets obvious that there are two different trends visible especially between 1 and 4 Hz. AC1, AC2, AC10, AC11, AC12 and ACR01 show very small amplification in the 1–4 Hz band, only factors between 1 and 2 are observed, whereas at higher frequencies at around 7 Hz, the amplification is more variable and increases up to 6 at AC3, AC4, AC5, AC6, AC7 and AC8. This variability at high frequencies reflects the variability of the disintegration in the near-surface part of the local structures. Site AC11 shows the lowest amplification at higher frequencies and we can assume that the rock has a low degree of disintegration. The stations AC3, AC4, AC5, AC6, AC7 and AC8 show a linear increase of the amplification factors between 0.5 and 2 Hz, with a more flat part between 2 and 4 Hz, with amplification factors of 3–5. For frequencies above 4 Hz, the amplification is site-dependent and varies between 5 and 15. The higher amplified stations (AC3, AC4, AC5, AC6, AC7 and AC8) are located very close, respectively, in the middle of the dense crack network. Here, the geological observation of strongly fractured rock mass corresponds well to the geophysical observation of higher amplification.

7 COMPARISON CUOLM DA VI AND ALP CASCHLÈ

In order to compare the SRSR between Alp Caschlè and Cuolm da Vi, the geometrical mean of the SRSR curves from the two sites are plotted together in Fig. 20. The blue curves are the results from Cuolm da Vi, while the red curves show the amplification at Alp Caschlè. Although the data were not acquired simultaneously and the reference conditions are not necessarily the same, the observed SRSRs show very similar patterns (compared to relative amplifications at other investigated unstable slopes in Switzerland), even though the instability Alp Cachlè is currently not moving. Therefore, one can conclude that the activity level of an unstable rock slope is not the key controling parameter of high amplification and that the degree of internal fracturation is the important factor. As known from geology, slope instabilities can undergo different states of activity like active, suspended, reactivated, inactive, dormant, abandoned, stabilized or relicted (Cooper 2007). However, if the slope is currently in an inactive state, the fractures—which have been developed during active times—are still there, reducing the stiffness of the rock mass and affecting the ground-motion amplification and polarization. On the one hand, the amplification at Alp Caschlè, in the part with large disintegration of the rock mass, is also slightly increasing with higher frequencies, but the gradient in the SRSR curves is not as steep as at Cuolm da Vi. On the other hand, at Alp Caschlè amplification in the fractured part starts at a lower frequency of 0.5 Hz. We might therefore expect a different gradient in the velocity profile at the two sites, and different properties of rock at depth (especially different disintegration of the rock). A smaller gradient in amplification might indicate less disintegration of the rock mass in a particular depth range at the site Alp Caschlè, when comparing to the site Cuolm da Vi.

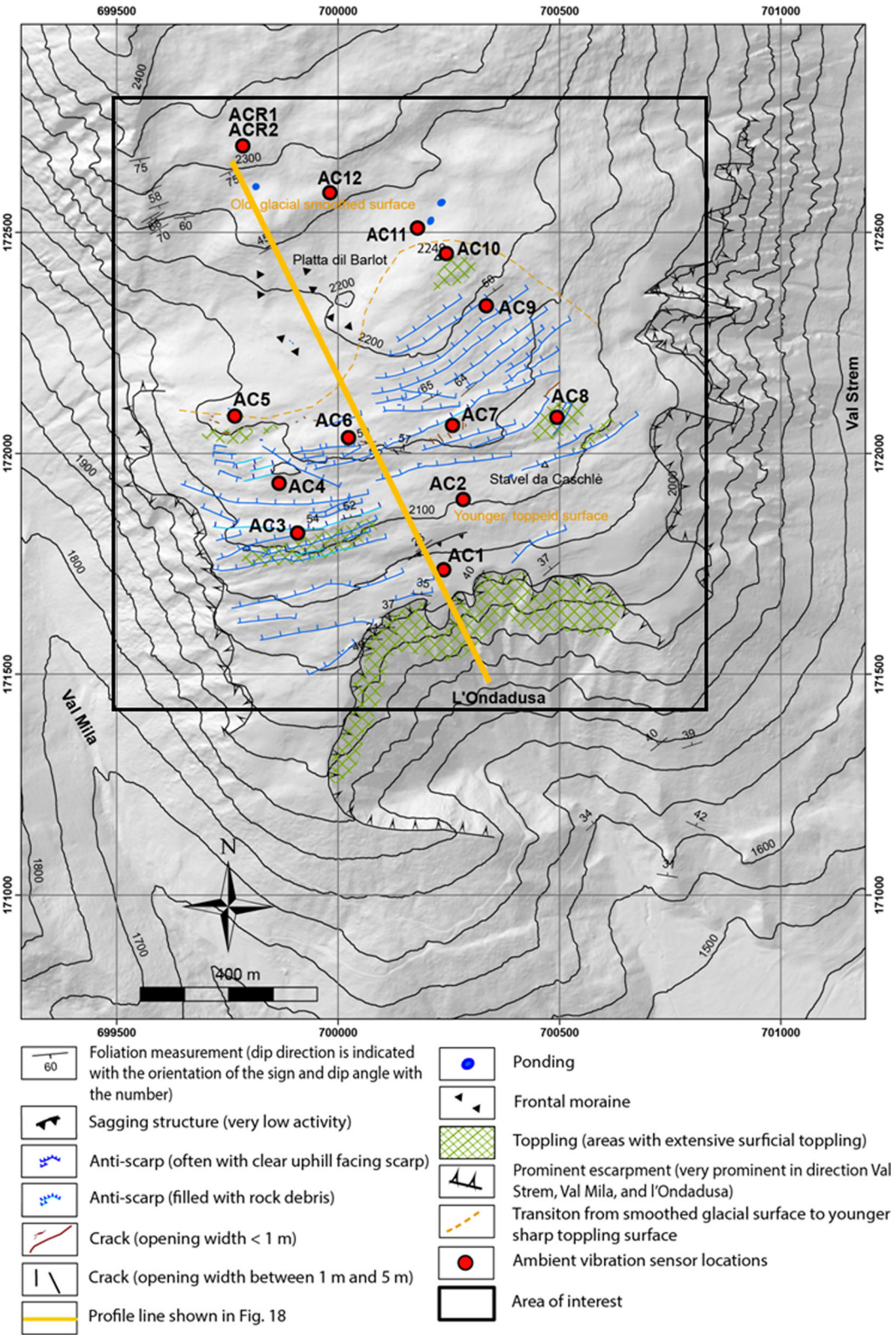

Figure 17. Map of Alp Caschlè indicating the structures induced by the moving rock slope.

At Alp Caschlè, low amplification is observed in the front area of the rock slope (AC1 and AC2) that is supposed to be part of an inactive sagging structure. This amplification curve is similar to the one's at Cuolm da Vi in subarray B, with amplifications being even lower at Alp Caschlè. We interpret the observations to be the effect of a block structure with less internal rock disintegration. These observations are quite surprising, as one expects generally higher amplifications closer to the cliff where the rock is not constrained and therefore has a higher freedom of movement.

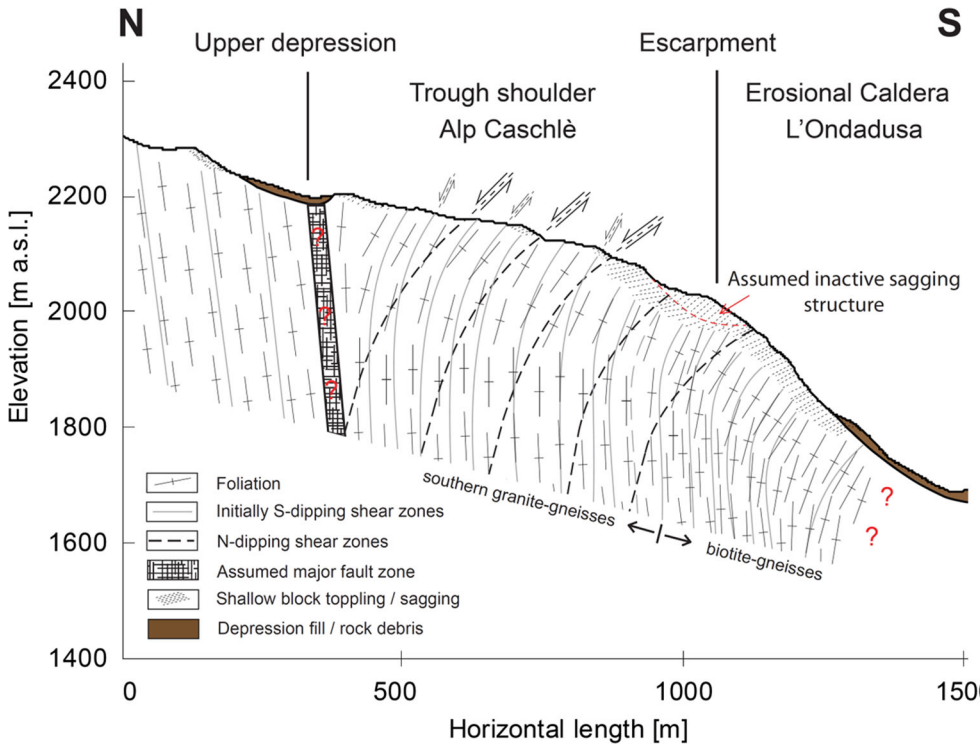

Figure 18. Profile of the site Alp Caschlè (Hugentobler 2015). The location of the profile can be seen in Fig. 17.

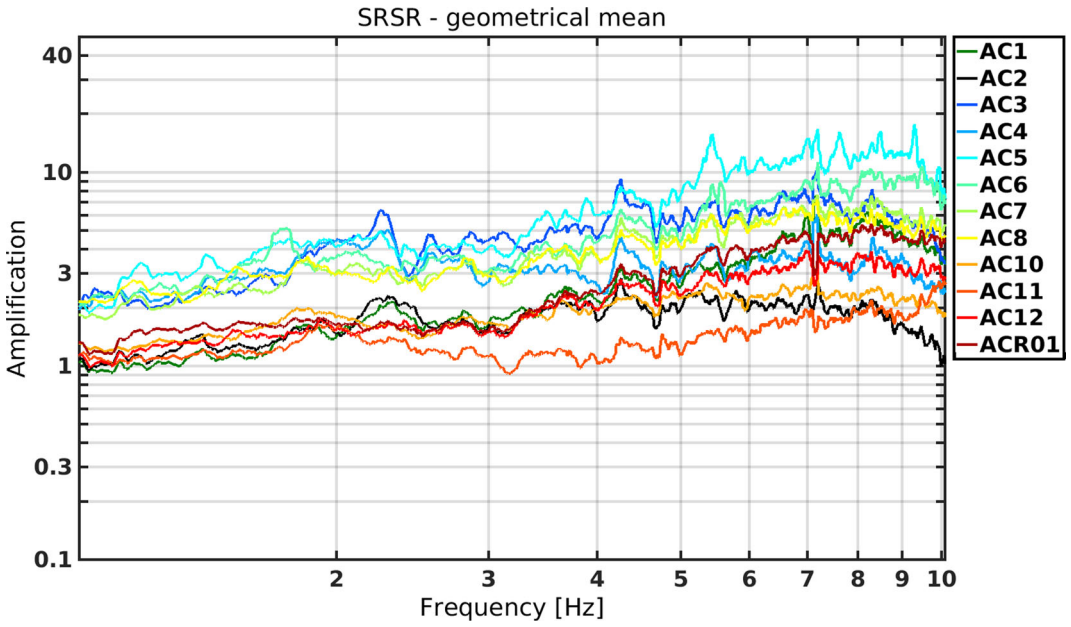

Figure 19. SRSR measured at Alp Caschlè. Two trends are visible between 1 and 4 Hz. Higher amplified stations are located in a highly fractured area and low amplified stations are located in areas showing less surface fracturing.

8 DISCUSSION AND CONCLUSIONS

In this study, the comparison of the seismic response of the sites Cuolm da Vi and Alp Caschlè is performed. Cuolm da Vi is a large (1.5 km^2) and active deep-seated rock slope instability. Alp Caschlé has very similar geological properties and tectonic settings. While Alp Caschlè has not been moving recently, Cuolm da Vi shows average displacements of 20 cm yr^{-1}. Nonetheless, both sites present a similar seismic response. The activity level of a slope does not seem to directly influence the seismic response for such kind of slopes. In contrast to studies by Burjánek *et al.* (2010a, 2012), no strong directionality is observed that can be linked to the slope deformation direction. This is mainly due to the disintegration of the rock material, decreasing with increasing depth. Therefore, seismic investigations deliver complementary information in addition to the displacement measurements in this case. The only link between the

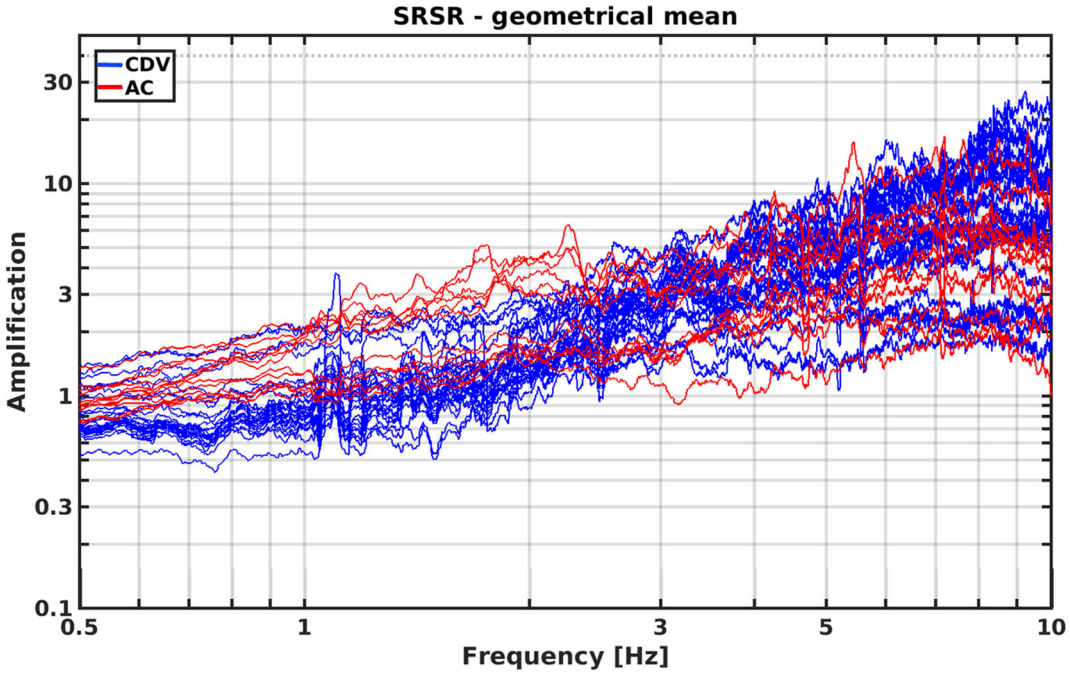

Figure 20. Comparison of the SRSR curves from Cuolm da Vi (blue) and Alp Caschlè (red). The amplification value represents the geometrical mean of the horizontal components.

displacements and the seismic vibrations is that the more a slope is moving the higher is the expected disintegration of the rock mass.

On one hand, TFPA and SRSR analysis at locations within the deep-seated instability of Cuolm da Vi reveal no common resonance frequency that can be related to the total depth of the instability. Only potential resonance frequencies of more local unstable masses are detected mostly close to open fractures. On the other hand, it is possible to retrieve surface wave dispersion curves and perform inversions for the shear wave velocity structure at Cuolm da Vi. The retrieved velocity profile shows a gradient with two visible changes in the slope (potential interfaces) at around 100 and 400–460 m. The change at 100 m can be related to the depth of the instability. No propagating surface waves are identified when open fractures impede their propagation. Such observations show that the complexity of the seismic response of unstable rock slopes depends on the internal structure of the rock mass. Cuolm da Vi represents a site where the low-frequency response (i.e. at wavelengths comparable to dimensions of the instability) is mostly influenced by the underlying, fractured rock strata, which can be characterized by a gradient shear wave velocity profile. Such profile might origin from a decreasing number or closing of the rock fractures with increasing depth. Based solely on ambient vibration observations, we can conclude that the failure mechanism is likely not controlled by a network of deep compliant fractures, but on the gradual disintegration of the rock mass. While the velocity gradient is observed in the larger part of the structure at Cuolm da Vi and detectable by a gradual increase of the observed ground-motion amplification between 1 and 10 Hz, we find specific areas where amplification is smaller and constant above 3 Hz. This indicates that the velocity gradient is only very smooth or absent for the intermediate depth range between 35 and 150 m. Such behaviour might be interpreted as a structure composed of blocks. This kind of observation is very similar at the lower part of both instabilities Cuolm da Vi and Alp Caschlè. It might be that these blocks are important in terms of stabilizing the instabilities—at least at some parts of Cuolm da Vi—and acting as a barrier.

A smoother increase in amplification is observed at Alp Caschlè, which can indicate less disintegration of the rock mass in a particular depth range at this site, when compared to the sites in subarray A of Cuolm da Vi, where a high level of disintegration is observed, due to the high activity at the slope.

The observed high-frequency polarization is attributed to the different failure mechanisms and movement orientations within the shallow part of the deep-seated instability of Cuolm da Vi, which causes strongly varying response characteristics at different locations. Strongest site effects (polarization and spectral amplification) within the instability of Cuolm da Vi are observed at locations with strongly disturbed superficial rock masses due to local extensions, close to prominent cracks or cliffs, or at very exposed locations within the instability. We estimate the depth of the largest open fractures to be at least around50 min subarray B, which is associated with the block thickness, and around 20 m in the upper part of the instability in subarray D.

It is difficult to find a proper reference station. Even when studying the geological map beforehand, the border between stable and instable is not always obvious. In such cases, one should always leave at least two stations fixed when measuring different configurations. Preferentially the fixed stations are relatively stable and can be used as backup reference stations. Redundant measuring points allow a reasonable comparison between recordings at different times. For example, it can be checked, if the noise level changes significantly due to varying anthropogenic noise or wind. Moreover, all the amplification levels reported in this study are only relative, with respect to unknown reference conditions. This can be overcome by permanent or semi-permanent installations of seismic stations, recording earthquake ground motion at the site of interest and in the regional seismic network (Edwards *et al*. 2013).

ACKNOWLEDGEMENTS

The research presented in this study is funded by ETH project ETH-1212–2 (Characterization of unstable rock slopes through passive seismic measurements). The GPS data are provided by Donatsch Ingenieure AG. Furthermore, we want to thank Christoph Nänni and Andreas Huwiler for constructive discussion and input.

REFERENCES

Abrecht, J., 1994. Geologic units of the Aar Massif and their pre-alpine rock associations—a critical review, *Schweiz. Mineral. Petrograph. Mitteil.,* **74**(1), 5–27.

Amann, F., 2005. Großhangbewegung Cuolm Da Vi (Graubünden, Schweiz)—Geologisch-geotechnische Befunde und numerische Untersuchungen zur Klärung des Phänomens, *unpublished dissertation,* Friedrich-Alexander-Universität Erlangen-Nürnberg.

Amann, F., Donatsch, G., Bonanomi, Y. & Moser, M., 2006. Kinematik und Bewegungsmechanismus der tiefgründigen Instabilität Cuolm Da Vi (Graubünden, Schweiz), *Bull. Angew. Geol*., **11**(2), 117–132.

Bonnefoy-Claudet, S., Cornou, C., Bard, P.-Y., Cotton, F., Moczo, P., Kristek, J. & Fäh, D., 2006a. H/V ratio: a tool for site-effects evaluation. Results from 1-D noise simulations, *Geophys. J. Int.,* **167**(2), 827–837.

Bonnefoy-Claudet, S., Cotton, F. & Bard, P.-Y., 2006b. The nature of noise wavefield and its applications for site-effects studies—a literature review, *Earth-Sci. Rev.,* **79**(3–4), 205–227.

Burjánek, J., Gassner-Stamm, G., Poggi, V., Moore, J.R. & Fäh, D., 2010a. Ambient vibration analysis of an unstable mountain slope, *Geophys. J. Int.,* **180**(2), 820–828.

Burjánek, J., Gassner-Stamm, G. & Fäh, D., 2010b. Array-measurements in the area of Visp and St. Niklaus, COGEAR deliverable 3.1.2, Swiss Seismological Service, Zürich, Switzerland, Report SED/COGEAR/R/003/20100226.

Burjánek, J., Moore, J.R., Yugsi Molina, F.X. & Fäh, D., 2012. Instrumental evidence of normal mode rock slope vibration, *Geophys. J. Int.,* **188,** 559–569.

Burjánek, J., Edwards, B. & Fäh, D., 2014. Empirical evidence of local seismic effects at sites with pronounced topography: a systematic approach, *Geophys. J. Int.,* **197**(1), 608–619.

Burjánek, J., Gischig, V., Moore, J. & Fäh, D., 2017. Ambient vibration characterization and monitoring of a rock slope close to collapse, *Geophys. J. Int.,* in press, doi:10.1093/gji/ggx424.

Capon, J., 1969. High resolution frequency wavenumber spectrum analysis, *Proc. IEEE,* **57,** 1408–1418.

Cooper, R.G., 2007. *Mass Movements in Great Britain, Geological Conservation Review Series,* Vol. 33, Joint Nature Conservation Committee, Peterborough, p. 348.

Del Gaudio, V. & Wasowski, J., 2010. Advances and problems in understanding the seismic response of potentially unstable slopes, *Eng. Geol.,* **122,** 73–83.

Del Gaudio, V., Muscillo, S. & Wasowski, J., 2014. What we can learn about slope response to earthquakes from ambient noise analysis: an overview, *Eng. Geol.,* **182,** 182–200.

Edwards, B., Michel, C., Poggi, V. & Fäh, D., 2013. Determination of site amplification from regional seismicity: application to the Swiss National Seismic Networks, *Seismol. Res. Lett.,* **84,** 611–621

Fäh, D., Stamm, G. & Havenith, H.-B., 2008. Analysis of three-component ambient vibration array measurements, *Geophys. J. Int.,* **172,** 199–213.

Frei, B. & Löw, S., 2001. Struktur und Hydraulik der Störzonen im südlichen Aar-Massiv bei Sedrun, *Eclogae geol. Helv.,* **94**(2001), 13–28.

Hugentobler, M., 2015. Slope kinematics and ambient vibration of the northern flank of the upper Vorderrheintal, *Master thesis*, ETH Zürich, Switzerland.

Joyner, W.B., Warrick, R.E. & Fumal, T.E., 1981. The effect of Quaternary alluvium on strong ground motion in the Coyote Lake, California, earthquake of 1979, *Bull. seism. Soc. Am.,* **71,** 1333–1349.

Kleinbrod, U., Burjánek, J. & Fäh, D., 2017. On the seismic response of instable rock slopes based on ambient vibration recordings, *Earth Planets Space*, **69,** 126, doi:10.1186/s40623-017-0712-5.

Kleinbrod, U., Burjánek, J. & Fäh, D., 2016. From ambient vibration assessment of potential rock slope instabilities to earthquake triggered rockslides, in *16WCEE: 16th World Conference on Earthquake Engineering,* Santiago, Chile, January 9–13, Paper no. 2216.

Poggi, V. & Fäh, D., 2010. Estimating Rayleigh wave particle motion from three-component array analysis of ambient vibrations, *Geophys. J. Int.,* **180**(1), 251–267.

Poggi, V., Edwards, B. & Fäh, D., 2011. Derivation of a reference shear-wave velocity model from empirical site amplification, *Bull. seism. Soc. Am.,* **101,** 258–274.

Prieto, G.A., Parker, R.L. & Vernon, F.L., 2009. A Fortran 90 library for multitaper spectrum analysis, *Comput. Geosci.,* **35,** 1701–1710.

Schneider, T.R., 1993. Gotthard-Basistunnel, Auswertung der Detailkartierung 1991/92, Bericht Nr. 425aa, Bundesamt für Verkehr.

Ustaszewski, M.E., Hampel, A. & Pfiffner, O.A., 2008. Composite faults in the Swiss Alps formed by the interplay of tectonics, gravitation and postglacial rebound: an integrated field and modelling study, *Swiss J. Geosci.,* **101**(1), 223–235.

Wathelet, M., 2008. An improved neighborhood algorithm: parameter conditions and dynamic scaling, *Geophys. Res. Lett.,* **35,** L09301, doi:10.1029/2008GL033256.

Wathelet, M., Jongmans, D., Ohrnberger, M. & Bonnefoy-Claudet, S., 2008. Array performances for ambient vibrations on a shallow structure and consequences over Vs inversion, *J. Seismol.,* **12,** 1–19.